ELSEVIER

Review

Modelling issues in zeolite based separation processes

R. Krishna *, R. Baur

Department of Chemical Engineering, University of Amsterdam, Nieuwe Achtergracht 166, 1018 WV Amsterdam, The Netherlands

Abstract

The Maxwell–Stefan (M–S) formulation is shown to be the most convenient and general way of describing diffusion within zeolite structures. This theory goes a long way to explain the observed various types of dependencies of the Fick diffusivity with sorbate loading. For mixture diffusion within zeolites, the M–S theory provides clues for the development of novel separation techniques that rely on diffusion selectivity. We illustrate this aspect by considering a number of practical applications in membrane permeation and chromatographic separations.
© 2003 Elsevier B.V. All rights reserved.

1. Introduction

Zeolitic materials are used as sorbents and catalysts in a variety of processes within the chemical, petroleum, petrochemical and food industries [1–8]. Zeolite crystals are incorporated into binders (such as amorphous aluminosilicate) and perhaps a diluent (typically a clay mineral), and used in the form of powder (in fluidized beds) or pellets (in fixed beds). Alternatively, zeolite crystals are coated on to a porous membrane support and used in (catalytic) membrane permeation devices.

Zeolite based separation processes are carried out either under steady state, unsteady state or cyclic conditions. Fixed bed adsorbers are typically operated under transient conditions. Zeolite membrane processes typically operate under steady state conditions. Simulated moving bed adsorbers operate under cyclic conditions. While many of the modelling issues are classical, special attention needs to be paid to the proper description of mixture sorption and diffusion. Sorption and diffusion are closely inter-twined and the proper description of the latter requires a clear understanding of the former.

Considerable progress has been made during the last decade in developing a general, continuum theory for describing diffusion of mixtures in zeolites, using the Maxwell–Stefan (M–S) formulation [9–14]. Our first major objective is to review these developments. The second objective of this review is to show how the M–S approach can be incorporated into the modelling and design of

---

* Corresponding author. Tel.: +31-20-5257007; fax: +31-20-5255604.

E-mail address: krishna@science.uva.nl (R. Krishna).

Nomenclature

b_i	parameter in the Langmuir adsorption isotherm (Pa^{-1})
$[B]$	square matrix of inverse Maxwell–Stefan coefficients (m^{-2} s)
c_i	molar concentration of species i ($mol\ m^{-3}$)
D_i	Fick coefficient of pure component i ($m^2\ s^{-1}$)
D^*	self-diffusivity ($m^2\ s^{-1}$)
$[D]$	matrix of Fick diffusivities ($m^2\ s^{-1}$)
$Đ_i$	Maxwell–Stefan diffusivity of species i in zeolite ($m^2\ s^{-1}$)
$Đ_{ij}$	Maxwell–Stefan diffusivity describing interchange between i and j ($m^2\ s^{-1}$)
f_i	fugacity of species i; $f_i = p_i$ for ideal gases (Pa)
F	fractional approach to equilibrium (–)
Fo	Fourier number, tD/r_c^2 (–)
k	mass transfer coefficient for intracrystalline diffusion ($m\ s^{-1}$)
k_B	Boltzmann constant ($1.38 \times 10^{-23}\ J\ molecule^{-1}\ K^{-1}$)
L	Length of packed bed (m)
L_i	Onsager coefficient of pure component i ($m^2\ s^{-1}$)
$[L]$	matrix of Onsager coefficients ($m^2\ s^{-1}$)
m	summation parameter defined in Eq. (30) (–)
N_i	molar or molecular flux of species i ($mol\ m^{-2}\ s^{-1}$ or molecules $m^{-2}\ s^{-1}$)
P	system pressure (Pa)
P_i^0	vapour pressure analog (Pa)
p_i	partial pressure of species i (Pa)
q_i	molar loading of component i ($mol\ kg^{-1}$)
$q_{i,sat}$	saturation loading of component i ($mol\ kg^{-1}$)
$\bar{q}_i$	average loading of component i ($mol\ kg^{-1}$)
r	radial distance coordinate (m)
r_c	radius of spherical crystal (m)
R	gas constant ($8.314\ J\ mol^{-1}\ K^{-1}$)
Sh	Sherwood number (–)
S	Sorption selectivity (–)
S_P	Permeation selectivity (–)
t	time (s)
T	absolute temperature (K)
u	absolute fluid velocity in packed bed ($m\ s^{-1}$)
u_0	interstitial fluid velocity in packed bed ($m\ s^{-1}$)
x_i	mole fraction of component i in the adsorbed phase (–)
y_i	mole fraction of component i in bulk vapour phase (–)
z	distance coordinate along membrane (m)

Greek letters

δ	thickness of membrane (m)
ε	porosity of packed bed (–)
ϕ	surface potential defined in Eq. (64) ($J\ m^{-3}$)
Γ	thermodynamic correction factor (–)
$[\Gamma]$	matrix of thermodynamic factors (–)
θ_i	fractional occupancy of component i (–)

Θ_i	molecular loading (molecules per unit cell or per cage)
$\Theta_{i,\text{sat}}$	saturation loading (molecules per unit cell or per cage)
μ_i	molar chemical potential (J mol^{-1})
ρ	density (number of unit cells per m^3 or kg m^{-3})
Subscripts	
A	referring to site A
B	referring to site B
1	component 1 in binary mixture
2	component 2 in binary mixture
mix	referring to mixture loading
sat	referring to saturation conditions
i,j	components in mixture
p	derivative at constant pressure
s	referring to surface of particle
Superscripts	
0	pure component parameter
Vector and Matrix Notation	
()	component vector
[]	square matrix

practical devices such as membrane permeation units and fixed bed adsorbers. We aim to demonstrate the shortcomings of simpler modelling approaches. We begin our review by considering the M–S formulation for single component diffusion in zeolites.

2. Single component diffusion in zeolites

2.1. Maxwell–Stefan and Fick formulations

The best way to formulate the diffusion of a single component in a zeolite, is to use the M–S framework for diffusion in a non-ideal binary fluid mixture made up of species 1 and 2. In the M–S theory we recognise that to effect relative motion between the species 1 and 2 in a fluid mixture we must exert a force on each species. This 'driving' force is the chemical potential gradient, $\nabla_{T,P}\mu_1$, determined at constant temperature (T) and pressure (p) conditions. This 'driving' force is balanced by friction between the diffusing species 1 and 2 in the binary mixture. The friction experienced by species 1 is proportional to the difference in the velocities of diffusion of species 1

and 2, ($\boldsymbol{u}_1 - \boldsymbol{u}_2$), and to the concentration of species 2, which can be taken to be the mole fraction x_2. The force balance on the species 1 takes the form:

$$-\nabla_{T,p}\mu_1 = \frac{RT}{\mathnormal{Đ}_{12}}x_2(\boldsymbol{u}_1 - \boldsymbol{u}_2) \qquad (1)$$

The term ($RT/\mathnormal{Đ}_{12}$) on the right hand side of Eq. (1) may be interpreted as the friction, or drag, coefficient. With this definition, the M–S diffusivity $\mathnormal{Đ}_{12}$ has the units (m^2 s^{-1}) and the physical significance of an inverse drag coefficient. Einstein [15] was among the first to use Eq. (1) in deriving a simple procedure to estimate the diffusivity of large spherical shaped molecules in liquids in the dilute solution limit by equating ($RT/\mathnormal{Đ}_{12}$) with the frictional drag coefficient experienced by flow of spheres in a viscous liquid. For more details of the physical background to Eq. (1) the reader is referred to the book by Wesselingh and Krishna [16].

For application to zeolites, we identify species 2 as the zeolite material (subscript Z). The diffusion velocity $\boldsymbol{u}_2 \equiv \boldsymbol{u}_Z = 0$ because the zeolite matrix does not move and in any event we are interested in the motion with respect to the zeolite. We need the analogue of the mole fractions x_i for zeolite

diffusion. For this purpose, we use the fractional occupancies, θ_1, defined by

$$\theta_1 \equiv \Theta_1/\Theta_{1,\mathrm{sat}} = q_1/q_{1,\mathrm{sat}} \tag{2}$$

where Θ_1 is loading expressed in molecules per unit cell (or per (super)cage for cage type zeolite topologies) and $\Theta_{1,\mathrm{sat}}$ is the saturation loading. Alternatively, the loadings may be expressed in terms of q_1 with the units mole per kilogram; $q_{1,\mathrm{sat}}$ is the saturation molar loading. The 'vacancy' within the zeolite, θ_Z is

$$\theta_Z = 1 - \theta_1 \tag{3}$$

When the zeolite is saturated with respect to the diffusant 1, there are no more vacant sites within the zeolite and so

$$\theta_Z = 0; \quad \theta_1 = 1; \quad \Theta_1 = \Theta_{1,\mathrm{sat}}; \quad q_1 = q_{1,\mathrm{sat}} \tag{4}$$

For diffusion of component 1 in zeolite (Z) we therefore re-write, Eq. (1) as

$$-\nabla_{T,p}\mu_1 = \frac{RT}{D_{1Z}}\theta_Z \boldsymbol{u}_1 \tag{5}$$

where D_{1Z} is the M–S diffusivity and μ_1 is the chemical potential of the sorbed species 1. As has been explained by Krishna [17], it is more conventional to use an alternative definition of the M–S diffusivity $D_1 \equiv D_{1Z}/\theta_Z$ in order to parallel the Dusty Gas Model for diffusion in porous media. With this modified definition we obtain

$$-\nabla_{T,p}\mu_1 = \frac{RT}{D_1}\boldsymbol{u}_1 \tag{6}$$

It is more practical to work in terms of fluxes, N_1, expressed in terms of molecules transported per square meter per second rather than the diffusion velocity:

$$N_1 \equiv \rho\Theta_1\boldsymbol{u}_1 \tag{7}$$

where ρ is the zeolite density expressed as the number of unit cells (or (super)cages) per m^3. Alternatively, we may use the molar fluxes, N_1, defined in terms of moles transported per square meter per second:

$$N_1 \equiv \rho q_1\boldsymbol{u}_1 \tag{8}$$

where ρ is the zeolite matrix density expressed in kilogram per m^3. We use the same nomenclature,

N_1, for the molecular and molar fluxes and, without loss of generality, we proceed with our development in terms of the 'molecular' variant and introduce Eq. (7) into Eq. (6) to obtain

$$N_1 = -\rho\Theta_1 D_1 \frac{1}{RT}\nabla_{T,p}\mu_1$$

$$\equiv -\rho\Theta_{1,\mathrm{sat}}D_1 \frac{\theta_1}{RT}\nabla_{T,p}\mu_1 \tag{9}$$

Assuming equilibrium between the sorbed species and the bulk fluid phase we have the following relationship for the chemical potential μ_1

$$\mu_1 = \mu_1^0 + RT \ \ln(f_1) \tag{10}$$

where μ_1^0 is the chemical potential in the chosen standard state and f_1 is the fugacity. For not too high system pressures the component partial pressure, p_1, can be used in place of the component fugacity, f_1, i.e. $f_1 \approx p_1$. The chemical potential gradients may be expressed in terms of the gradient of the fractional occupancy, $\nabla\theta_1$:

$$\frac{1}{RT}\nabla\mu_1 = \frac{1}{\theta_1}\Gamma\nabla\theta_1;$$

$$\Gamma \equiv \theta_1\frac{\partial \ln f_1}{\partial\theta_1} \equiv \frac{\partial \ln f_1}{\partial \ln\theta_1} \equiv \frac{\partial \ln f_1}{\partial \ln\Theta_1} \tag{11}$$

where Γ is the thermodynamic 'correction' factor. Introducing Eq. (11) into Eq. (9) yields

$$N_1 = -\rho D_1\Gamma\nabla\Theta_1 \equiv -\rho\Theta_{1,\mathrm{sat}}D_1\Gamma\nabla\theta_1 \tag{12}$$

The commonly used Fick formulation for zeolite diffusion is

$$N_1 = -D_1\nabla\Theta_1 \equiv -\rho\Theta_{1,\mathrm{sat}}D_1\nabla\theta_1 \tag{13}$$

where D_1 is the Fick diffusivity. The inter-relationship between the M–S and Fick diffusivities is

$$D_1 = D_1\Gamma; \quad D_1 = \frac{D_1}{\Gamma} \tag{14}$$

In the zeolite diffusion literature the M–S diffusivity D_1 is referred to as the 'corrected' diffusivity and the Fick diffusivity D_1 is also called the 'transport' diffusivity. The correction factor Γ can be determined from the sorption isotherm, after differentiation.
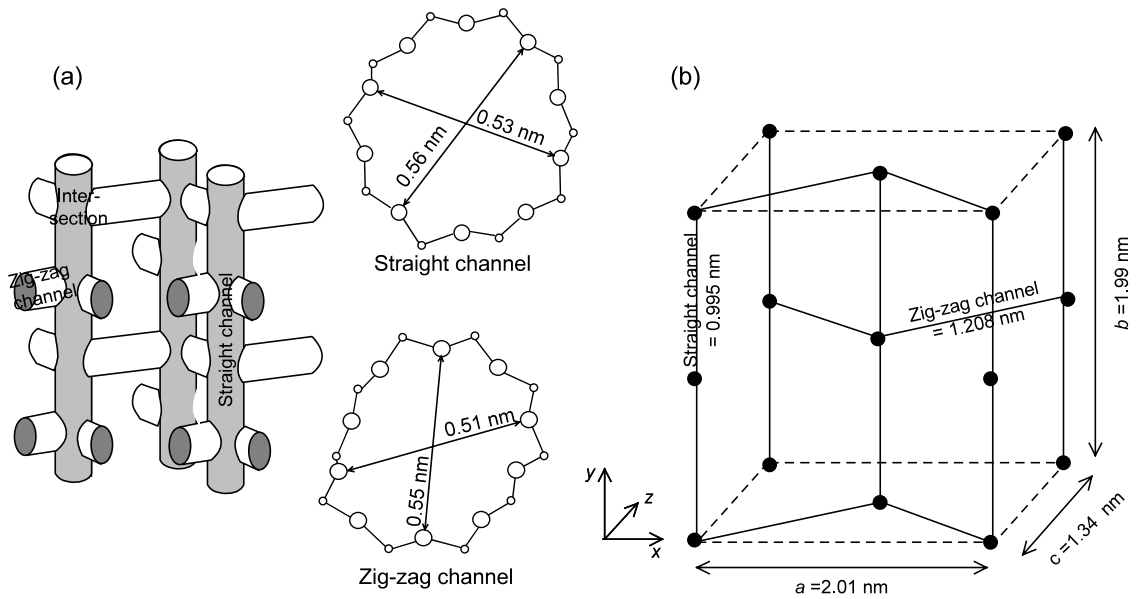
Fig. 1. (a) Schematic of structure of silicalite-1 (MFI). (b) Diffusion unit cell for silicalite-1 connecting intersection sites (large black dots) via straight and zig–zag channels. The crystallographic data were obtained from Atlas of Zeolite Framework Types of the International Zeolite Association (http://www.iza-online.org).

In order to obtain insights into zeolite diffusion, let us begin by considering diffusion of methane in silicalite-1, which is the all silica form of MFI zeolite. Fig. 1 shows a schematic of the structure of silicalite-1 that consists of a system of intersecting channels composed of zig–zag channels along x, cross-linked by straight channels along y. Both channels are defined by 10-rings. The straight
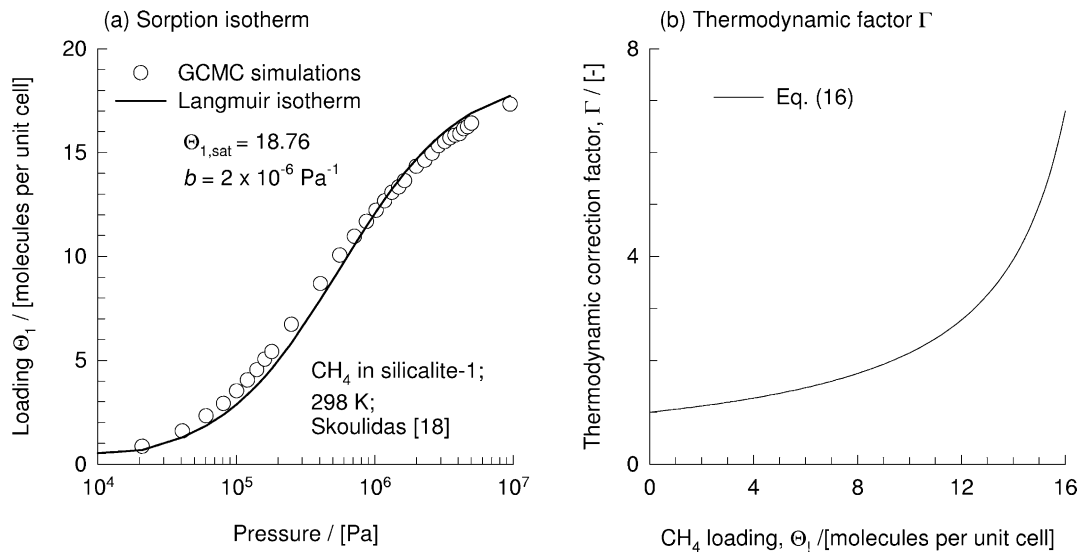

Fig. 2. (a) Sorption isotherm for CH_4 in silicalite-1 at 298 K. GCMC simulations of Skoulidas and Sholl [18]. (b) Thermodynamic correction factor.
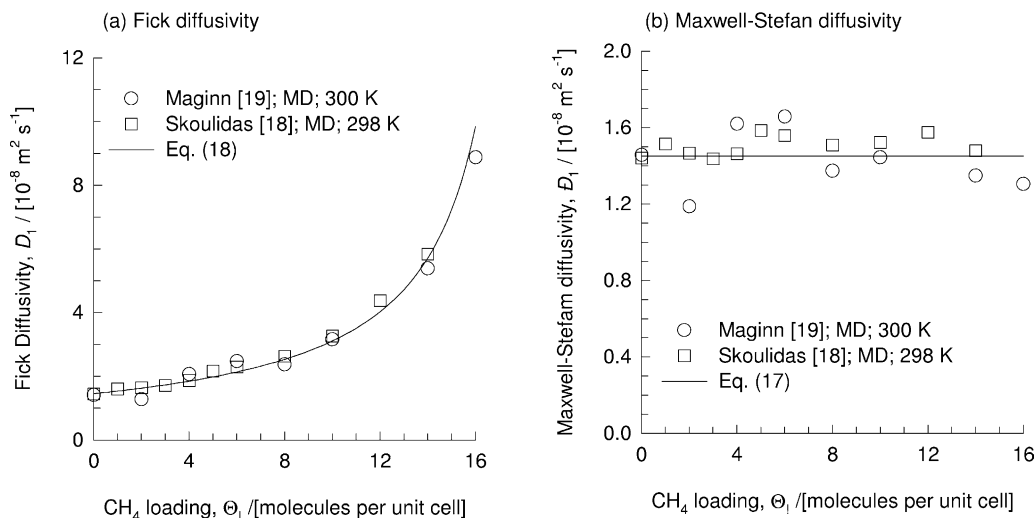
Fig. 3. (a) Fick diffusivity for CH_4 in silicalite-1 at 298 and 300 K as a function of molecular loading. MD simulation data of Skoulidas and Sholl [18] and Maginn et al. [19]. (b) Maxwell–Stefan diffusivity for CH_4 as function of molecular loading.

channels are approximately elliptical in shape having a 0.53×0.56 nm^2 cross section while the zig–zag channels have a 0.51×0.55 nm^2 cross section. First, let us consider the sorption isotherm data of Skoulidas and Sholl [18] for CH_4 at 298 K. As shown in Fig. 2(a), the grand canonical Monte Carlo (GCMC) simulations of the component loadings are represented very well with the simple Langmuir isotherm

$$\Theta_1 = \frac{\Theta_{sat} b_1 p_1}{1 + b_1 p_1}; \quad \theta_1 = \frac{b_1 p_1}{1 + b_1 p_1} \qquad (15)$$

with the saturation loading $\Theta_{1,sat}$ fitted with a value of 18.76 molecules per unit cell [19]. Skoulidas and Sholl [18] have used a virial equation of state in order to account for gas phase non-idealities. Heyden et al. [20] have stressed the importance of taking account of gas phase non-idealities in interpreting GCMC simulation results for sorption of light gases, and their mixtures. The determination of $\Theta_{1,sat}$ from MC simulations is subject to some uncertainty and a value of 19 was obtained by Krishna and Paschek [13]. The thermodynamic correction factor Γ can be calculated from Eq. (11) to obtain

$$\Gamma = \frac{1}{1 - \Theta_1/\Theta_{sat}} = \frac{1}{1 - \theta_1} \qquad (16)$$

and these are shown in Fig. 2(b). We note the sharp increase in Γ as the saturation loading is approached.

The molecular dynamics (MD) simulations for the Fick diffusivity D_1 of CH_4 in MFI [18,19] are shown in Fig. 3(a). The Fick D_1 is seen to increase sharply when Θ_1 approaches the saturation value. On the other hand, the M–S diffusivity $Đ_1$, calculated from D_1 using Eq. (14) is seen to be practically independent of loading; see Fig. 3(b). Therefore the M–S diffusivity at any loading can be estimated from the zero-loading M–S diffusivity $Đ_1(0)$ using

$$Đ_1 = Đ_1(0) \qquad (17)$$

Skoulidas and Sholl [21] have found the relation Eq. (17) to be valid also for diffusion of He, Ar and Ne in MFI; this scenario is typical of *weakly confined* molecules in zeolite hosts. When scenario Eq. (17) prevails, the Fick diffusivity increases sharply with loading, following:

$$D_1 = \frac{Đ_1}{1 - \theta_1} = \frac{Đ_1(0)}{1 - \theta_1} \qquad (18)$$

and this is indeed verified by the MD simulations; see Fig. 3(a).

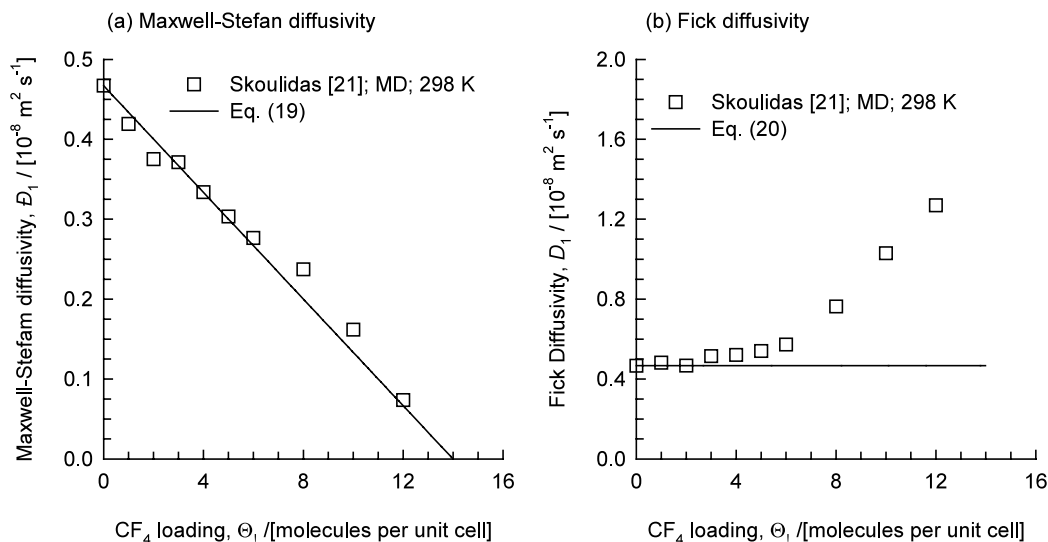For diffusion of other guest molecules, such as CF_4 and SF_6 in MFI a different loading depen-

Fig. 4. (a) Maxwell–Stefan diffusivity for CF_4 as function of molecular loading. (b) Fick diffusivity for CF_4 in silicalite-1 at 298 K as a function of molecular loading. MD simulation data of Skoulidas and Sholl [18].

dence of $Đ_1$ has been observed by Skoulidas and Sholl [21]. As seen in Fig. 4(a), the MD simulation results of Skoulidas and Sholl [18,21] for CF_4 in silicalite-1, shows that $Đ_1$ decreases strongly with the loading and follows the relation

$$Đ_1 = Đ_1(0)(1 - \Theta_1/\Theta_{1,\text{sat}}) = Đ_1(0)(1 - \theta_1) \qquad (19)$$

where the $\Theta_{1,\text{sat}}$ is *fitted* with a value of 15 molecules per unit cell. The scenario Eq. (19) is typical of *strongly confined* molecules in zeolite hosts.

If the Langmuir isotherm holds, the Fick diffusivity should be independent of loading, i.e.

$$D_1 = \frac{Đ_1}{1 - \theta_1} = Đ_1(0) \qquad (20)$$

The MD simulated D_1 for CF_4 in silicalite-1 follows Eq. (20) for loadings below about 6 molecules; see Fig. 4(b). For higher loadings the MD simulated D_1 values are higher than anticipated by Eq. (20) due to adsorbate–adsorbate interactions. Whether a molecule follows scenario Eq. (18) or Eq. (20) depends on the degree of confinement within the zeolite host, and on adsorbate–adsorbate interactions.

2.2. Estimating zero-loading diffusivities

Mechanistically, the M–S diffusivity $Đ_i$ may be related to the displacement of the adsorbed molecular species ℓ, and the jump frequency, or transition probability v, which in general can be expected to be dependent on the total occupancy [22,23]. For a square lattice, the zero-loading diffusivity can be estimated from

$$Đ_i(0) = \frac{1}{4} v \ell^2 \qquad (21)$$

where the jump probability in the x- and y-directions are taken to be identical. Similarly, for a cubic lattice we obtain

$$Đ_i(0) = \frac{1}{6} v \ell^2 \qquad (22)$$

For the MFI topology (Fig. 1), Kärger [24] has derived the following set of relations for the diffusivities in the x, y and z directions:

$$Đ_x(0) = \frac{1}{4} v_{zz} a^2; \quad Đ_y(0) = \frac{1}{4} v_{\text{str}} b^2;$$

$$Đ_z(0) = \frac{1}{4} \frac{v_{\text{str}} v_{zz}}{v_{zz} + v_{zz}} c^2 \qquad (23)$$

where v_{str} and v_{zz} are the jump frequencies for movement along the straight (str) and zig–zag (zz) channels, respectively and the dimensions a, b and c are as specified in Fig. 1. The Kärger formula given by Eq. (23) is however restricted in its applicability to molecules which are predominantly located at the intersections. For specific molecules, the zero-loading diffusivity $Đ_i(0)$ can be determined experimentally. Alternatively, the jump frequencies can be estimated by use of transition state theory [25–29]. Consider for example diffusion of 2-methylhexane (2MH) in MFI zeolite. Using the transition rate theory, Smit et al. [28] determined the jump frequencies (i.e. hopping rates) along the straight and zig–zag channels to be $v_{str} = 1.4 \times 10^5$; $v_{zz} = 5 \times 10^4$ s^{-1}. Substituting these values along with the dimensions $a = 2.01$; $b = 1.99$; $c = 1.34$ nm into the formula Eq. (23) we obtain the zero-loading diffusivities in the x, y and z directions as $Đ_x(0) = 5.05 \times 10^{-14}$; $Đ_y(0) = 13.9 \times 10^{-14}$; $Đ_z(0) = 0.827 \times 10^{-14}$ m^2 s^{-1}. These values correspond extremely well with results obtained from KMC simulations with the jump frequencies v_{str} and v_{zz} as input, as indeed they should. The *average* zero-loading diffusivity for MFI topology can be obtained from

$$Đ_i(0) = \frac{1}{3}(Đ_x(0) + Đ_y(0) + Đ_z(0))$$
$$= 6.58 \times 10^{-14} \ m^2 s^{-1} \tag{24}$$

which value again coincides with those from KMC simulations for diffusion of 2MH [30]. The 2MH molecules are located exclusively at the intersections and therefore the Kärger formula Eq. (23) is applicable.

For smaller molecules such as CH$_4$ that are located not only at the intersections but also in the channel interiors, the formula Eq. (23) breaks down. In order to illustrate this let us consider the KMC simulations results for pure component CH$_4$ in MFI at 300 K performed by Paschek and Krishna [31]. The jump frequency along the straight channels is taken as $v_{str} = 4.2 \times 10^{11}$ s^{-1}; for transport along the zig–zag channels $v_{str} = 3.6 \times 10^{11}$ s^{-1}. The number of sorption sites within the MFI lattice is taken to be 24, higher than the saturation loading that is about 19 molecules per unit cell. From Eq. (23) we calculate $Đ(0)$ to be 2.75×10^{-7} m^2 s^{-1}, whereas the KMC simulations [31] yield a considerably lower value of $Đ(0)$ 1.5×10^{-8} m^2 s^{-1}.

2.3. Transient uptake; adsorption vs. desorption

When the Fick diffusivity D_1 follows the strongly non-linear behaviour described by Eq. (18), adsorption and desorption processes exhibit strong asymmetry. During the uptake, or adsorption, process the Fick diffusivity increases as time progresses, i.e. with loading. Conversely, during the desorption process the Fick diffusivity decreases as time progresses and, therefore, proceeds considerably more slowly than adsorption. To illustrate this let us consider transient uptake of ethane into a spherical zeolite crystallite of 4A zeolite; the uptake is described by the following partial differential equation

$$\frac{\partial q_1}{\partial t} = \frac{1}{\rho} \frac{1}{r^2} \frac{\partial}{\partial r}(r^2 N_1) \tag{25}$$

where r is the radial distance coordinate and the following initial and boundary conditions:

initial condition: $t = 0$; $0 < r < r_c$; $q_1 = q_{1,0}$; $\theta_1 = \theta_{1,0}$ (26)

boundary (surface) condition: $t = 0$; $r = r_c$; $q_1 = q_{1,s}$; $\theta_1 = \theta_{1,s}$ (27)

Here $q_{i,0}$ is the initial loading and $q_{1,s}$ is the loading that is equilibrium with the bulk fluid phase. The M–S diffusivity of ethane in 4A zeolite is taken as $Đ_1/r_c^2 = 2.45 \times 10^{-4}$ s^{-1} following Garg and Ruthven [32]. The method of lines [33] was used to solve the set of equations Eqs. (18), (25) and (26) and Eq. (27) and the results are presented in Fig. 5 where the y-axis represents the fractional approach to equilibrium F, defined as

$$F \equiv (\bar{q}_1 - q_{1,0})/(q_{1,s} - q_{1,0}) \tag{28}$$

where $\bar{q}_1$ is the average loading within the particle at any time t, defined by

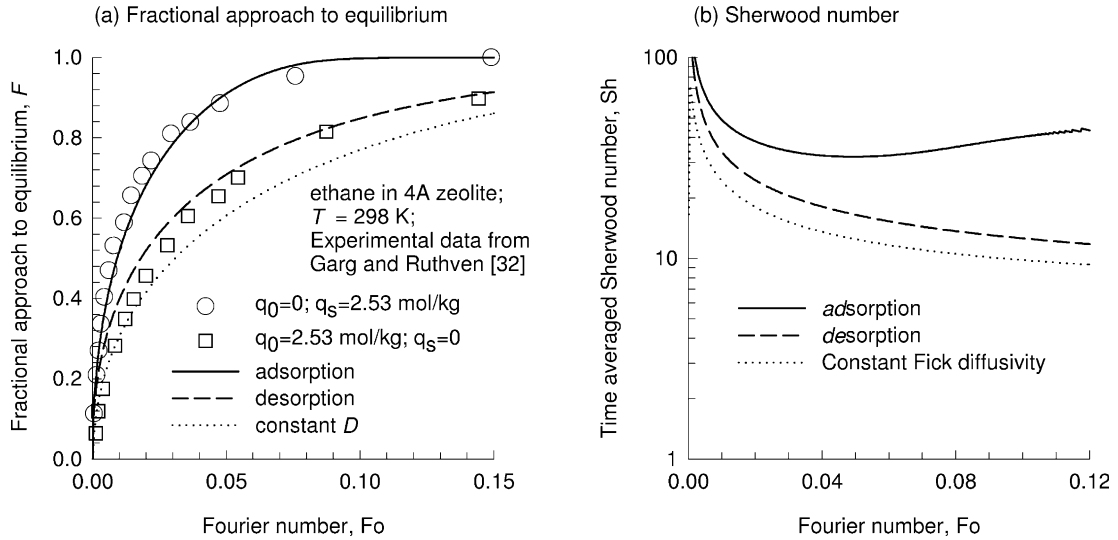$$\bar{q}_1 = \frac{3}{r_c^3} \int_0^{r_c} q_1 r^2 dr \tag{29}$$

Fig. 5. (a) Adsorption and desorption kinetics for ethane in 4A zeolite. Experimental data from Garg and Ruthven [32]. The simulation results with $Đ_1/r_c^2 = 2.45 \times 10^{-4} \, \text{s}^{-1}$. (b) Time-averaged Sherwood number as function of the Fourier number.

As can be seen in Fig. 5, there is excellent agreement between the experiments of Garg and Ruthven [32] and the simulation results. Also, the results shown in Fig. 5 confirm the asymmetry in *adsorption* and *desorption* kinetics, with the latter being significantly slower.

If the Fick diffusivity is independent of the loading, Eq. (25) can be solved analytically to obtain

$$\frac{(\bar{q}_1 - q_{1,0})}{(q_{1,x} - q_{1,0})} \equiv F$$

$$= 1 - \frac{6}{\pi^2} \sum_{m=1}^{\infty} \frac{\exp\left(-m^2\pi^2 \dfrac{D_1}{r_c^2}t\right)}{m^2} \tag{30}$$

For comparison purposes, this constant-D solution is also plotted in Fig. 5(a) with a dotted line. It is clear that thermodynamic correction factor, has a significant influence on adsorption and desorption rates.

The time-averaged Sherwood number Sh, a dimensionless number describing diffusion within the zeolite crystals, can be calculated from the fractional approach to equilibrium

$$Sh \equiv \frac{k(2r_c)}{D} = -\frac{2}{3\left(\dfrac{D_1}{r_c^2}t\right)} \ln (1 - F) \tag{31}$$

where k is the mass transfer coefficient for intracrystalline diffusion. For detailed derivation of Eq. (31), see Clift et al. [34]. The variation of Sh for the constant diffusivity model is shown in Fig. 5(b). In the adsorption literature a constant value of $Sh = 10$, corresponding to a 75% approach to equilibrium, is usually taken to model uptake in batch adsorbers and breakthrough curves in packed beds. This assumption is usually referred to as the linear driving force (LDF) approximation [4,6,7]. In general, the LDF approach is not appropriate for modelling of zeolitic adsorption because of the strong dependence of the Fick diffusivity on the loading. Taking the non-linear character of the Fick diffusivity (using Eq. (18)), the Sh number can be significantly higher than 10; this is seen by comparison from the values obtained from the numerical solutions presented in Fig. 5(a). We do not recommend the use of the LDF approximation for modelling of zeolite based processes.

If the Fick diffusivity follows the strong confinement scenario Eq. (20) instead of the weak confinement scenario Eq. (18), the constant-D
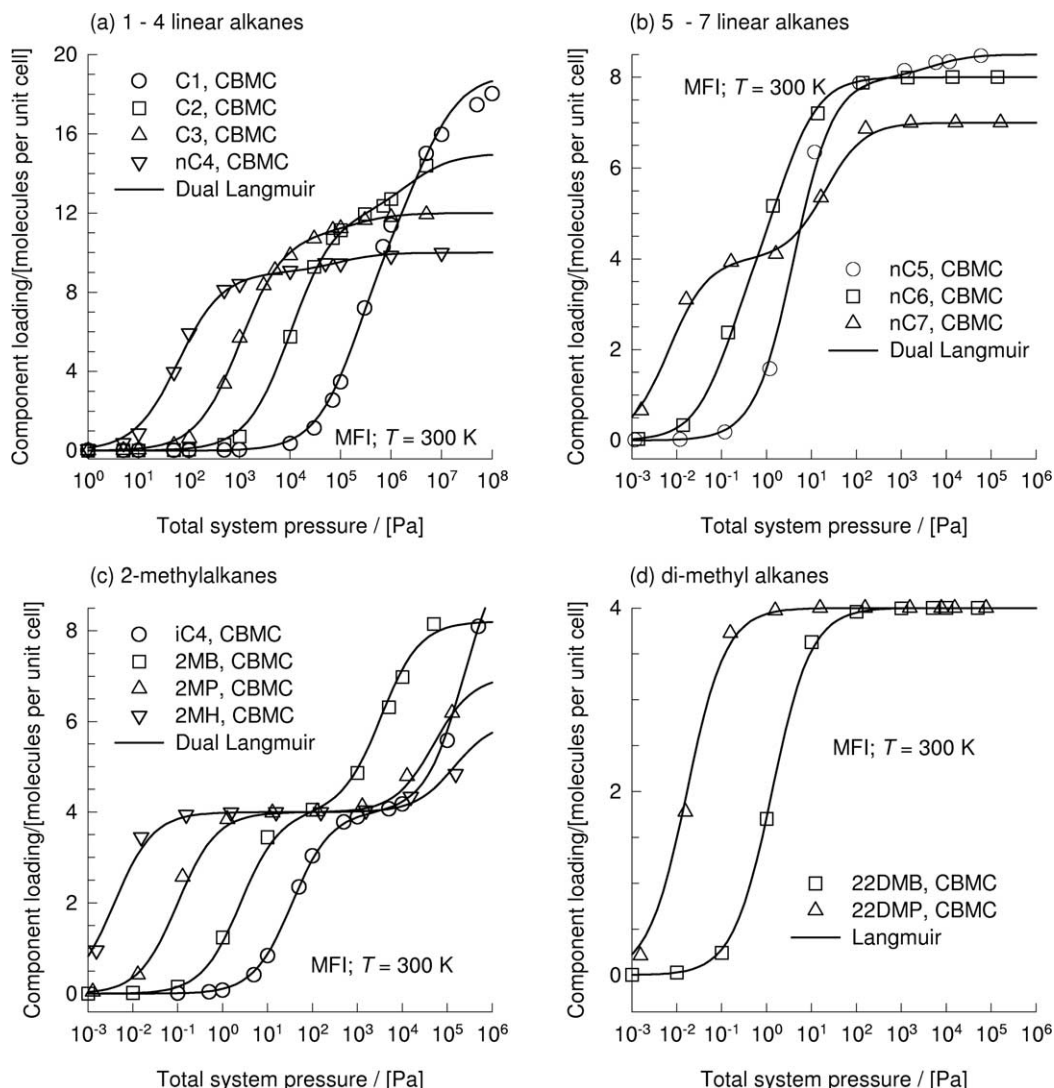
Fig. 6. Pure component isotherms for linear, 2-methyl and di-methyl alkanes in MFI at 300 K calculated using CBMC simulations. The continuous lines represent the fits of the isotherms using the DSL model with parameters given in Table 1.

solution Eq. (30) is valid; for this case the LDF approximation is a good one. Also, in cases where macropore/mesopore diffusion resistances are present, the non-linearities of intracrystalline zeolite diffusion are diluted and the LDF approximation may be a good one. The reader is referred to the paper by Sircar and Hufton [35], illustrating cases for which the LDF model is a good approximation.

2.4. Isotherm inflection influence

In the foregoing discussions we have used the Langmuir isotherm to describe the sorption isotherm; in many cases the isotherms exhibit inflection behaviour. Configurational-bias Monte Carlo (CBMC) simulations of the isotherms of linear and branched alkanes in the 1–7 C atom range at 300 K in MFI zeolite are shown in Fig. 6; the CBMC

simulation technique has been described in detail in publications by Smit, Krishna and co-workers [13,36–49]. Strictly speaking the x-axes of the data shown in Fig. 6 refer to the fugacities of the components, as these are the entities that are calculable from the chemical potentials that are used in GCMC simulations. Normal heptane shows a pronounced inflection at a loading of $\Theta = 4$. Normal hexane shows a slight inflection at this loading due to 'commensurate freezing' effects [50]. All 2-methyl alkanes show inflection behaviour (Fig. 6(c)); this is because these molecules prefer to locate at the intersections between straight and zig–zag channels, which offers more 'leg-room'. At $\Theta = 4$ all intersections are fully occupied. To locate the 2-methyl alkanes within the channel interiors requires an extra push, leading to inflection behaviour. The 2,2dimethylbutane (2,2DMB) and 2,2dimethylpentane (2,2DMP) molecules are too bulky to be located at the channel interiors and both molecules show a maximum (saturation) loading of 4 (Fig. 6(d)).

The regularity of the zeolite pore structure makes these adsorbents especially convenient for application of statistical thermodynamics [2] to model the isotherms. The method is best suited to those zeolites where the structure consists of more or less discrete cages interconnected through
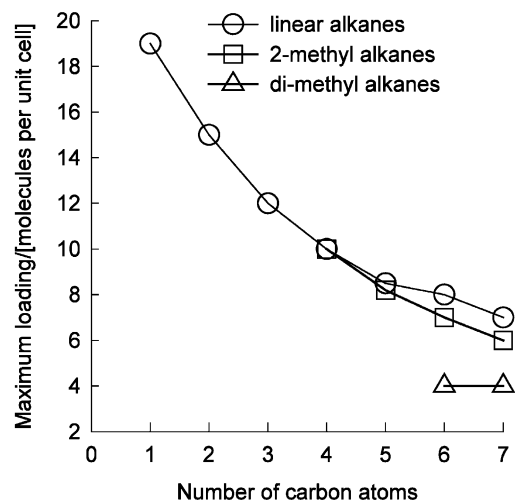

Fig. 7. (a) Maximum saturation loadings of linear, 2-methyl and di-methyl alkanes in MFI at 300 K. NVT calculations at 300 K described in Ref. [40].

relatively small windows. The Langmuir isotherm can be derived as a limiting case of the statistical model. To account for the observed inflection behaviour we adopt the Dual-site Langmuir (DSL) model. In this model the loading $\Theta_1^0(P)$, expressed in molecules per unit cell is expressed as a function of the pressure P as follows:

Table 1
DSL parameters for alkanes in MFI at 300 K

| Component	Dual Langmuir parameters			
	Site A		Site B	
	$b_{i,A}$ (Pa^{-1})	$\Theta_{i,sat,A}$ (molecules per unit cell)	$b_{i,B}$ (Pa^{-1})	$\Theta_{i,sat,B}$ (molecules per unit cell)
C$_1$	4.86×10^{-6}	11.0	2.38×10^{-7}	8.0
C$_2$	9.73×10^{-5}	12.0	4.38×10^{-7}	3.0
C$_3$	9.64×10^{-4}	11.0	5.06×10^{-6}	1.0
nC$_4$	1.63×10^{-2}	9.0	1.14×10^{-5}	1.0
nC$_5$	0.25	8.0	2×10^{-4}	0.5
2MB	0.4	4.0	3×10^{-4}	4.2
nC$_6$	7.0	4.0	0.4	4.0
2MP	10.0	4.0	2.0×10^{-5}	3.0
2,2DMB	0.76	4.0	–	0
nC$_7$	150	4.0	5×10^{-2}	3.0
2MH	260	4.0	7×10^{-6}	2.0
2,2DMP	60	4.0	–	0

The fits correspond to CBMC simulations [48].
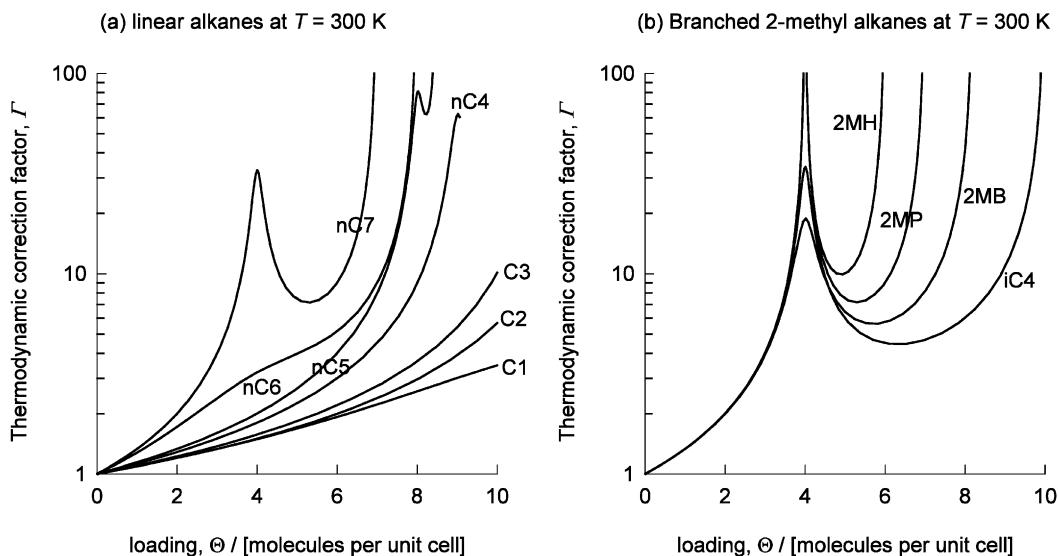
Fig. 8. (a) Thermodynamic factor for (a) linear alkanes and (b) 2-methyl alkanes in MFI at 300 K calculated using the DSL model. DSL parameters given in Table 1.

$$\Theta_1^0(P) \equiv \Theta_{1,A} + \Theta_{1,B}$$

$$= \frac{\Theta_{1,sat,A} b_{1,A} P}{1 + b_{1,A} P} + \frac{\Theta_{1,sat,B} b_{1,B} P}{1 + b_{1,B} P} \qquad (32)$$

The superscript 0 on $\Theta_1^0(P)$ is used to emphasize that the relation is for pure component loadings. In Eq. (32) $b_{1,A}$ and $b_{1,B}$ represent the DSL model parameters expressed in Pa^{-1} and the subscripts A

and B refer to two sorption sites within the MFI structure, with different sorption capacities and sorption strengths. The $\Theta_{i,sat,A}$ and $\Theta_{i,sat,B}$ represent the saturation capacities of sites A and B, respectively. The fitted parameters for the pure component isotherms, shown in Fig. 6, are listed in Table 1. It is to be noted that the total saturation loading $\Theta_{1,sat} = \Theta_{1,sat,A} + \Theta_{1,sat,B}$ is not a fitted parameter but taken from the final plateau value
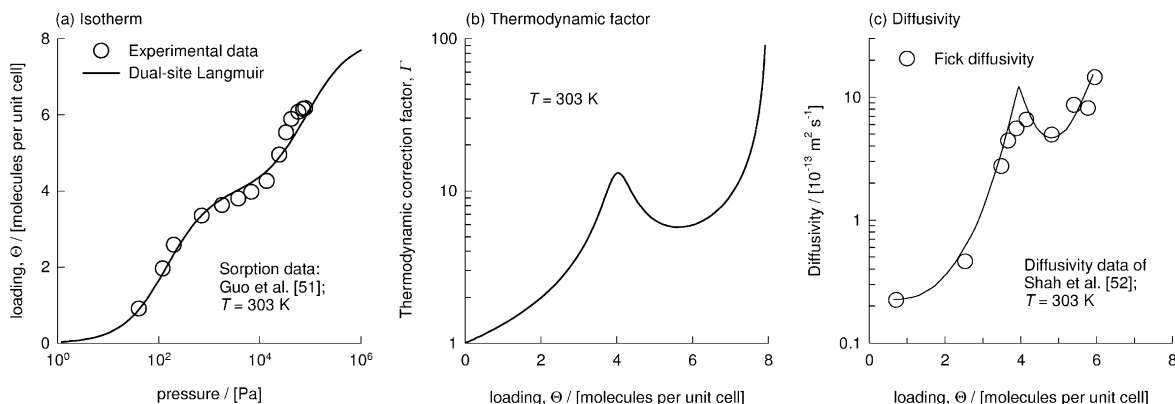

Fig. 9. (a) Pure component isotherms for sorption of benzene on MFI at a temperature of 303 K. Experimental data from Guo et al. [51]. The DSL model parameters are $\Theta_{sat,A} = 4$, $\Theta_{sat,B} = 4$, $b_{1,A} = 7 \times 10^{-3}$ Pa^{-1}, $b_{1,B} = 1.2 \times 10^{-5}$ Pa^{-1}. (b) The thermodynamic correction factor calculated using the DSL model. (c) Fick diffusivity data for benzene in MFI at 303 K. Data from Shah et al. [52].

Table 2
DSL parameters for C_5, C_6 alkane isomers in MFI at 362 K

Component	Temperature (K)	Dual Langmuir parameters			
		Site A		Site B	
		$b_{i,A}$ (Pa^{-1})	$\Theta_{i,sat,A}$ (molecules per unit cell)	$b_{i,B}$ (Pa^{-1})	$\Theta_{i,sat,B}$ (molecules per unit cell)
nC_5	362	8.15×10^{-3}	4.0	4.19×10^{-4}	4.3
nC_6	362	6.32×10^{-2}	4.0	1.7×10^{-3}	4.0
3MP	362	4.75×10^{-2}	4.0	2.27×10^{-5}	2.3
2,2DMB	362	1.085×10^{-2}	4.0	2.27×10^{-5}	0.0

The fits correspond to CBMC simulations [13,43,45,89].

of the sorption isotherm, estimated from CBMC simulations. In general the saturation loading decreases with increasing C number and with increased degree of branching; see Fig. 7.

The thermodynamic correction factor for the DSL model is

$$\Gamma = \frac{1}{\dfrac{\Theta_{1,A}}{\Theta_1}\left(1 - \dfrac{\Theta_{1,A}}{\Theta_{1,sat,A}}\right) + \dfrac{\Theta_{1,B}}{\Theta_1}\left(1 - \dfrac{\Theta_{1,B}}{\Theta_{1,sat,B}}\right)}$$

(33)

Calculations of the thermodynamic correction factor for linear and 2-methyl alkanes are shown in

Fig. 8. The thermodynamic correction factor for nC_7 and all 2-methyl alkanes shows two extrema: a maximum at the inflection point $\Theta = \Theta_{1,sat,A} = 4$ and a minimum at a loading $\Theta_{1,sat,A} < \Theta < \Theta_{1sat,A} + \Theta_{1,sat,B}$.

The isotherm inflection for 2-methyl alkanes is due to preferential location of molecules at the intersection. Inflection behaviour is also exhibited by benzene in MFI at $T = 303$ K due to phase transitions [51] (Fig. 9(a)). Since the Fick diffusivity is proportional to the thermodynamic factor, it can be expected to also exhibit two extrema (Fig. 9(b)). This is indeed verified by the experimental data of Shah et al. [52]; see Fig. 9(c).
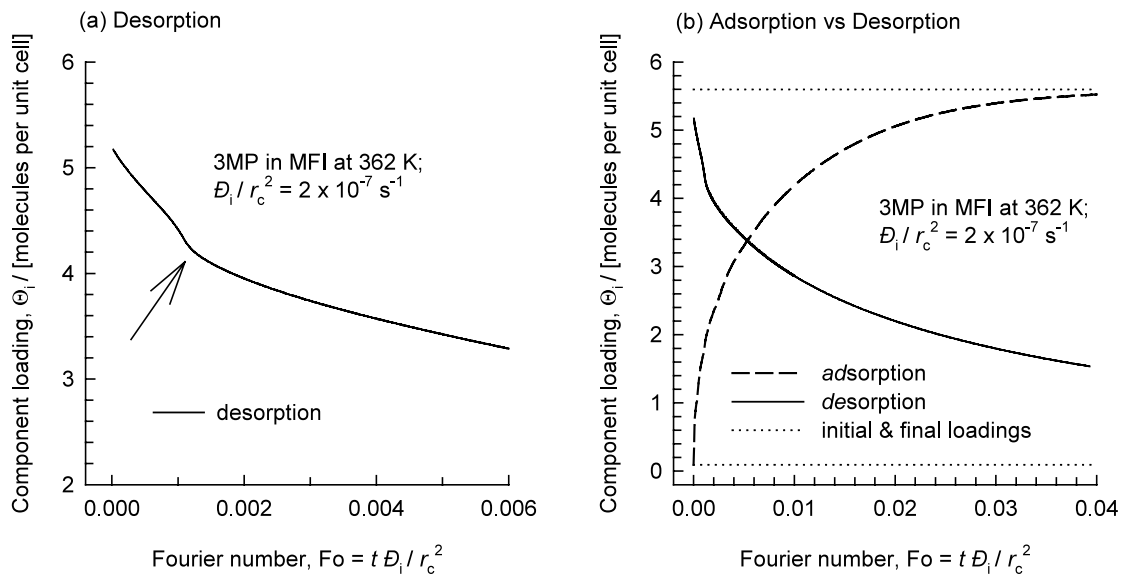

Fig. 10. (a) Kinetics of desorption of 3MP in MFI at 362 K. (b) Comparison of adsorption and desorption kinetics for 3MP.
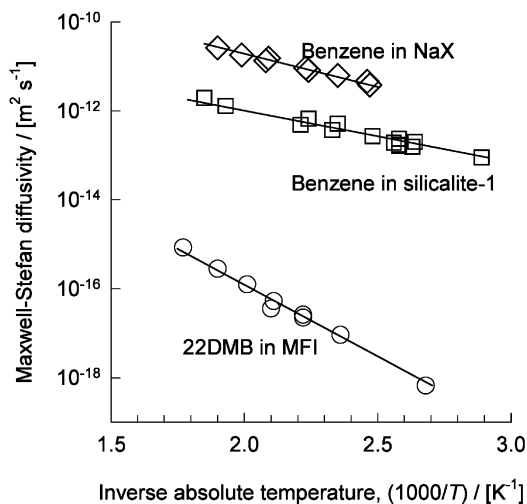
Fig. 11. Arrhenius plot for the Maxwell–Stefan diffusivity. Various data sources cited in the review by Ruthven and Post [5].

In order to illustrate the influence of isotherm inflection on the uptake characteristics, let us consider desorption of 3-methyl pentane (3MP) from MFI zeolite at a temperature of 362 K. The DSL isotherm parameters, obtained from CBMC simulations [13,41], are specified in Table 2. Initially the crystals are equilibrated by exposing to surrounding 3MP vapour at a pressure $p_{1,0} = 100$ kPa. The equilibrium loading within MFI is

uniform and $\Theta_{1,0} = 5.596$ molecules per unit. At time $t = 0$, the surface of the zeolite crystals is exposed to 3MP vapour at a partial pressure $p_{1,s} = 0.5$ Pa, which gives an equilibrium loading at the outer surface $\Theta_{1,s} = 0.093$. Numerical solution of the partial differential equation Eq. (25), with the initial and boundary conditions given by Eq. (26) and Eq. (27) yields the $\Theta_1(t)$ shown in Fig. 10(a). We note an inflection in the desorption kinetics, indicated by the arrow. Fig. 10(b) compares the desorption and adsorption kinetics of 3MP. The desorption kinetics are much slower than the adsorption kinetics; this is evidenced by the fact that at $Fo \equiv Ð_1 t/r_c^2 = 0.04$, the adsorption process is nearly at equilibrium whereas the desorption process has still a long way to go to equilibration.

A three-site model for sorption of aromatics on ZSM-5 has been proposed by Szabelski et al. [53] in order to account for two inflection points observed under certain temperature conditions. This three-site model is shown to be essential in order to describe the observed loading dependence of the diffusivity [53].

2.5. Temperature dependence of M–S diffusivity

Diffusion within a zeolite structure is an activated process and this is evidenced by the fact that the M–S diffusivity follows an Arrhenius tem-
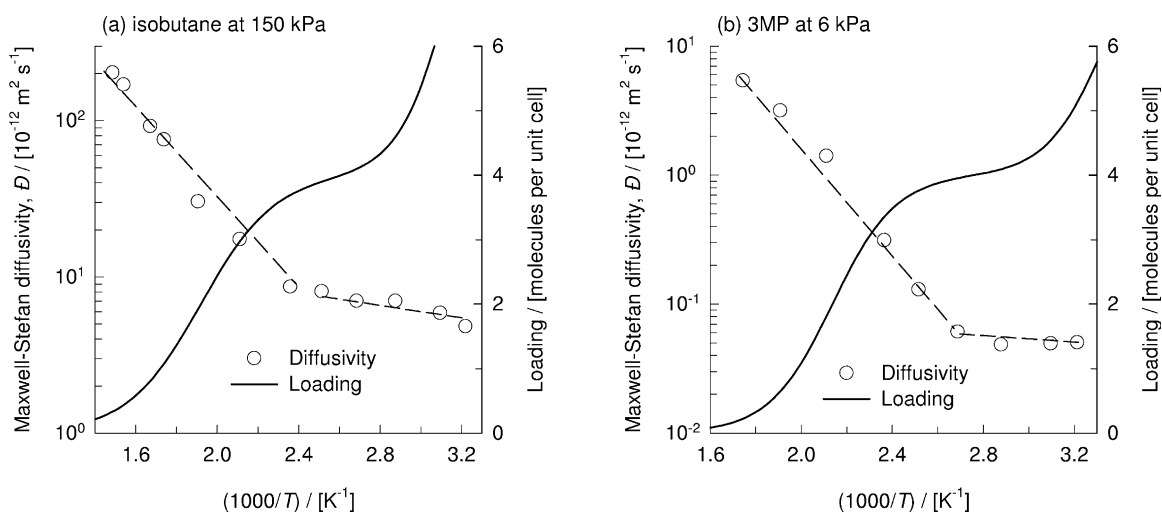

Fig. 12. Arrhenius plot for the Maxwell–Stefan diffusivity of (a) isobutane and (b) 3MP in silicalite-1. Experimental data of Millot et al. [54,55]. Also shown with continuous lines are the sorption loadings.

(a) Loading < 4 molecules per unit cell   (b) Loading > 4 molecules per unit cell
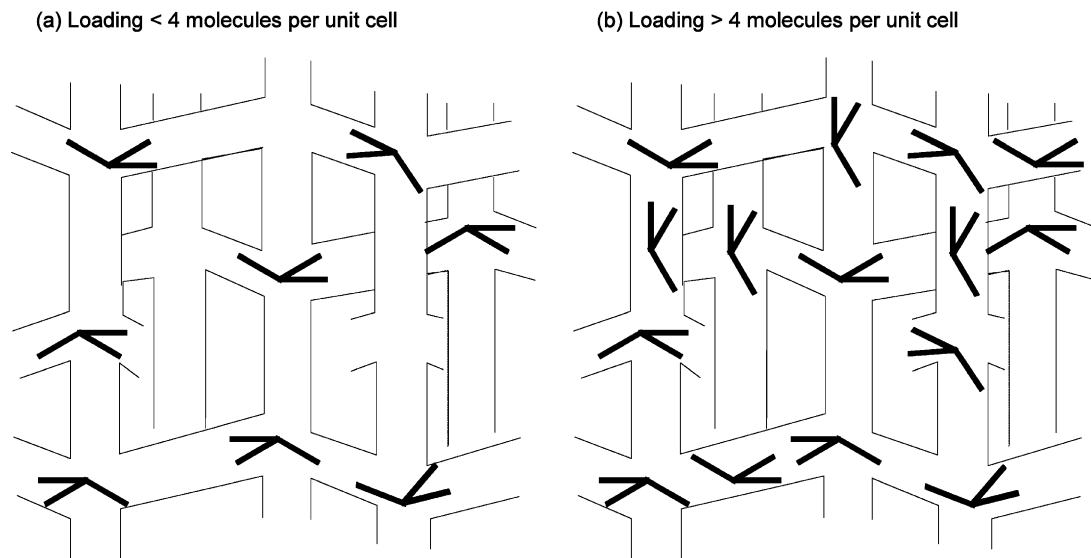

Fig. 13. Schematic showing the siting of isobutane molecules within MFI at (a) $\Theta < 4$, and (b) $\Theta > 4$ molecules per unit cell.

perature dependence, as is evidenced by the experimental data shown in Fig. 11.

For branched alkanes, such as iso-butane (iC_4) and 3MP, the M–S diffusivity data of Millot et al. [54,55] show a change in the slope of the $\log(Đ)$ vs. $1/T$ data at a certain temperature; see Fig. 12. In order to understand the change in the slope, we have plotted the sorption loadings of the iC_4 and 3MP as a function of T at the prevailing system pressures. We note that the change in the activation energy occurs precisely at a loading Θ of 4 molecules per unit cell. To rationalize the observations, consider the siting of iC_4 molecules at loadings (a) $\Theta < 4$, and (b) $\Theta > 4$ molecules per unit cell; see Fig. 13(a). As shown by Vlugt et al. [38], for $\Theta < 4$, iC_4 occupies the intersection sites exclusively. Since the iC_4 molecules are far removed from each other, they do not exert any intermolecular repulsion. At $\Theta = 4$, the intersections are fully occupied and in order to achieve $\Theta > 4$, the iC_4 molecules need to be forced into the channel interiors (straight or zig–zag channels); see the schematic in Fig. 13(b). The iC_4 molecules are now in closer proximity and therefore repulsive forces come into play. Paschek and Krishna [56] performed kinetic Monte Carlo (KMC) simulations for diffusion of iC_4 in silicalite-1 to demon-

strate that even small repulsive forces experienced at $\Theta > 4$, is sufficient to cause a significant change in the slope of the $\log(Đ)$ vs. $1/T$ curve. A similar story holds for 3MP.

3. Modelling mixture diffusion with the Maxwell–Stefan formulation

3.1. Fick and Onsager approaches

For n-component diffusion the fluxes N_i are related to the gradients of the fractional occupancies by the generalization of Fick's law:

$$(N) = -\rho[\Theta_{\mathrm{sat}}][D](\nabla\theta) \tag{34}$$

where $[D]$ is the n-dimensional square matrix of Fick diffusivities; $[\Theta_{\mathrm{sat}}]$ is a diagonal matrix with elements $\Theta_{i,\mathrm{sat}}$, representing the saturation loading of species i. The fractional occupancies θ_i are defined by the generalization of Eq. (2):

$$\theta_i \equiv \Theta_i/\Theta_{i,\mathrm{sat}} = q_i/q_{i,\mathrm{sat}}; \quad i = 1, 2, \ldots n \tag{35}$$

The estimation of the $n \times n$ elements of $[D]$ is complicated by the fact that these are influenced not only by the species mobilities (i.e. diffusivities $Đ_i$) but also by the sorption thermodynamics. In

setting up a proper mixture diffusion theory we need to use chemical potential gradients as the proper driving forces. In the irreversible thermo-dynamics (IT) treatment of zeolite diffusion, following the classical treatment of Onsager for intraphase diffusion in bulk fluid phases, the following linear constitutive relations are postu-lated by several researchers [57–62], ignoring coupling between mass diffusion and heat conduc-tion

$$(N) = -\rho[\Theta_{\text{sat}}][L]\frac{1}{RT}(\nabla\mu) \quad (36)$$

where $(\nabla\mu)$ is the column matrix of chemical potential gradients; $[L]$ is the square matrix of Onsager coefficients having the units $(\text{m}^2\,\text{s}^{-1})$. The Onsager matrix $[L]$ is non-diagonal, in gen-eral, and the cross-coefficients portray the cou-pling between species diffusion. The Onsager reciprocal relations demand that the matrix $[L]$ be symmetric, i.e.

$$L_{ij} = L_{ij}; \quad i,j = 1, 2, \ldots n \quad (i \neq j) \quad (37)$$

The chemical potential gradients in Eq. (36) may be expressed in terms of the gradients of the occupancies by introduction of the matrix of thermodynamic factors $[\Gamma]$

$$\frac{\theta_i}{RT}\nabla\mu_i = \sum_{j=1}^{n}\Gamma_{ij}\nabla\theta_j;$$
$$\Gamma_{ij} \equiv \left(\frac{\Theta_{j,\text{sat}}}{\Theta_{i,\text{sat}}}\right)\frac{\Theta_i}{f_i}\frac{\partial f_i}{\partial\Theta_j} \equiv \frac{\theta_i}{\theta_j}\frac{\partial\ln f_i}{\partial\ln\theta_j}; \quad (38)$$
$$i,j = 1, 2, \ldots n$$

where f_i is the fugacity of component i. Knowledge of the sorption isotherm is sufficient to allow estimation of $[\Gamma]$ and $(\nabla\mu)$. If the n-component sorption can be described by the multicomponent Langmuir isotherm, the elements of $[\Gamma]$ are given by

$$\Gamma_{ij} = \delta_{ij} + \frac{\theta_i}{1 - \theta_1 - \theta_2 \ldots - \theta_n}; \quad (39)$$
$$i,j = 1, 2, \ldots n$$

where δ_{ij} is the Kronecker delta. Strictly speaking from thermodynamic consistency arguments, the

multicomponent Langmuir isotherm can only be used when the saturation capacities of all the individual components in the mixture are identical.

Combining Eq. (36) and Eq. (38) we obtain

$$(N) = -\rho[\Theta_{\text{sat}}][L]\begin{bmatrix} 1/\theta_1 & 0 & 0 \\ 0 & \ddots & 0 \\ 0 & 0 & 1/\theta_n \end{bmatrix}[\Gamma](\nabla\theta) \quad (40)$$

Comparing Eq. (34) and Eq. (40) we obtain the inter-relation:

$$[D] = [L]\begin{bmatrix} 1/\theta_1 & 0 & 0 \\ 0 & \ddots & 0 \\ 0 & 0 & 1/\theta_n \end{bmatrix}[\Gamma] \quad (41)$$

The Fick matrix $[D]$ can be estimated from knowledge of the Onsager matrix $[L]$. In general the thermodynamic correction factor matrix $[\Gamma]$ is non-diagonal and this makes multicomponent diffusion in zeolites a strongly coupled process.

3.2. Maxwell–Stefan formulation

Unfortunately the IT theory provides no funda-mental guidelines for estimating $[L]$ from data on pure component transport coefficients. For esti-mating $[D]$ it is more convenient to adopt the M–S formulation, entirely consistent with the theory of IT, in which the chemical potential gradients are written as linear functions of the fluxes [11,12,14,63–65]:

$$-\rho\frac{\theta_i}{RT}\nabla\mu_i = \sum_{\substack{j=1 \\ j \neq i}}^{n}\frac{\Theta_j N_i - \Theta_i N_j}{\Theta_{i,\text{sat}}\Theta_{j,\text{sat}}\text{Đ}_{ij}} + \frac{N_i}{\Theta_{i,\text{sat}}\text{Đ}_i}; \quad (42)$$
$$i = 1, 2, \ldots n$$

When $n = 1$, Eq. (42) collapses to Eq. (9), and there is only one M–S diffusivity Đ_i; this is the pure component diffusivity of component i. For the general case we have to reckon with two types of M–S diffusivities: Đ_i and Đ_{ij}. The Đ_i are the same as encountered for pure component diffu-sion; these coefficients depend on the loading following e.g. Eq. (17) or Eq. (19). The Đ_{ij} serve to quantify correlative diffusion effects. Site-to-site jump leaves behind a vacancy; see the pictorial representation in Fig. 14 of jumps in the MFI and

(a) MFI structure
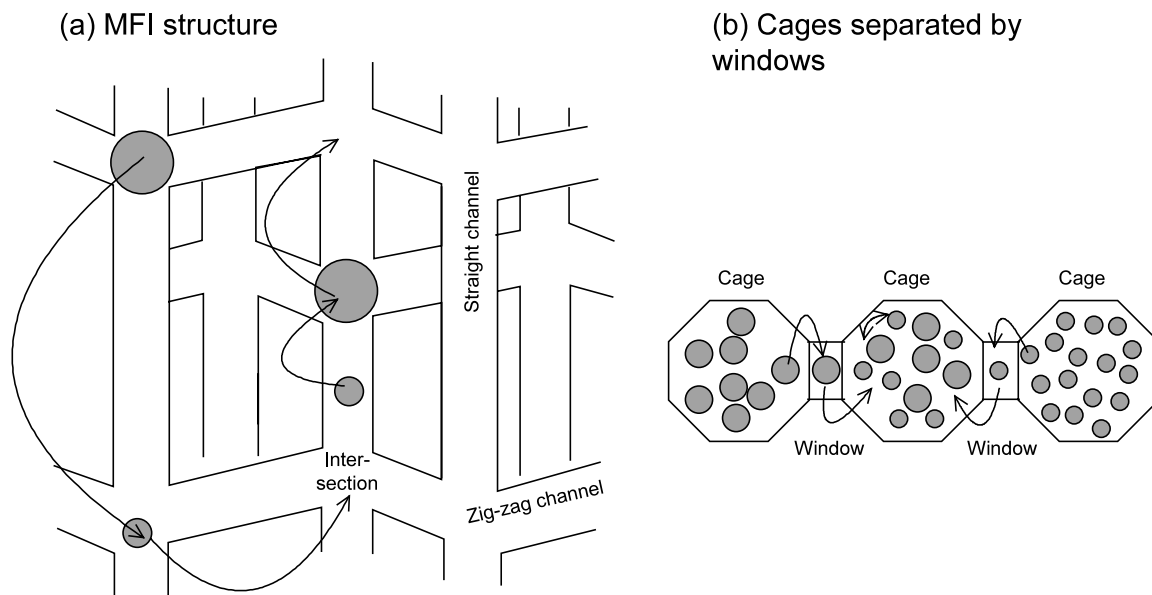
(b) Cages separated by windows

Fig. 14. Pictorial representation of the molecular jumps in (a) MFI structure, and (b) cages separated by windows.

cage topologies. Subsequent jumps are more likely to fill this vacancy, thus producing 'vacancy correlation' effects. For a clear discussion on correlation effects in diffusion we refer the reader to the recent review by Kärger et al. [66]. When the jump of species i creates a vacancy and this vacancy is filled by species j, the vacancy correlation effect is captured by the term containing the 'exchange' coefficients $Đ_{ij}$ in Eq. (42). The Onsager reciprocal relations demand $Đ_{ij} = Đ_{ji}$. The net effect of this exchange is a slowing down of a faster moving species due to interactions with a species of lower mobility. Also, a species of lower mobility is accelerated by interactions with another species of higher mobility. When the jump of species i creates a vacancy and this vacancy is filled by species i itself, the correlation effect is described by $Đ_{ii}$; this must be expected to be identical to the pure component M–S diffusivity $Đ_i$. For intersecting channel structures such as MFI (Fig. 14(a)) the interchange process takes place predominantly at the channel intersections. In structures such as LTA and FAU, molecule–molecule exchange takes place predominantly within the cages (Fig. 14(b)).

For estimation of the $Đ_{ij}$, Krishna and Wesselingh [11] suggested the logarithmic interpolation formula

$$Đ_{ij} = [Đ_i]^{\theta_i/(\theta_i+\theta_j)}[Đ_j]^{\theta_j/(\theta_i+\theta_j)} \tag{43}$$

based on the empirical approach of Vignes [67] for describing the concentration dependence of the diffusivity in a binary liquid mixture using as inputs the infinite dilution diffusivity values. The transition state theory was later used by Cullinan [68] to provide a theoretical basis to the Vignes approach. If we apply Eq. (43) to estimate the exchange coefficient of component i with itself, we obtain $Đ_{ii} = Đ_i$, the pure component diffusivity of i; we shall need this result below for estimation of the self-diffusivity.

We now try to inter-relate the M–S formulation with the Onsager and Fick formulations; to do this we define a n-dimensional square matrix $[B]$ with elements

$$B_{ii} = \frac{1}{Đ_i} + \sum_{\substack{j=1 \\ j \neq i}}^{n} \frac{\theta_j}{Đ_{ij}}; \quad B_{ij} = -\frac{\theta_i}{Đ_{ij}};$$

$$j = 1, 2 \ldots n \tag{44}$$

With this definition of $[B]$, Eq. (42) can be cast into n-dimensional matrix form:

$$(N) = -\rho[\Theta_{sat}][B]^{-1}[\Gamma](\nabla\theta) \qquad (45)$$

which gives the following expressions for the Onsager and Fick matrices

$$[L] = [B]^{-1}\begin{bmatrix} \theta_1 & 0 & 0 \\ 0 & \ddots & 0 \\ 0 & 0 & \theta_n \end{bmatrix}; \quad [D] = [B]^{-1}[\Gamma] \qquad (46)$$

For single component diffusion, Eq. (46) simplifies to Eq. (14). Eqs. (44) and (46) shows that the interchange coefficients $Đ_{ij}$, portraying correlated molecular jumps, will influence all the elements of $[L]$ and $[D]$. Put another way, the main elements of the Onsager matrix L_{ii} cannot be identified with pure component diffusion coefficients, as has been erroneously suggested in the literature by Sundaram and Yang [61]. In general, the Fick $[D]$ matrix has large non-diagonal elements and, consequently, the flux of any species i is strongly coupled to that of all other diffusing species j in the mixture.

For facile particle–particle exchange, i.e. $Đ_{ij} \rightarrow \infty$, vacancy correlation effects tend to get washed out. Facile counter-exchange of particles could occur, for example, within the cages of FAU and LTA zeolites when intra-cage hopping rates are high. We see from Eqs. (44) and (46) that when $Đ_{ij} \rightarrow \infty$, both $[B]$ and $[L]$ matrices reduce to diagonal matrices and the flux relations Eq. (42) simplify to give:

$$N_i = -\rho\Theta_{i,sat}\frac{L_{ii}}{RT}\nabla\mu_i \equiv -\rho\Theta_{i,sat}Đ_i\frac{\theta_i}{RT}\nabla\mu_i; \qquad (47)$$
$$i = 1, 2, \ldots n$$

The off-diagonal elements of the Onsager matrix are also a reflection of (vacancy) correlation effects and the assumption of vanishing off-diagonal elements of $[L]$ signifies vanishing correlation effects. The set of equations Eq. (47), with the

multicomponent Langmuir model to estimate mixture isotherms (Eq. (39)) were first developed by Habgood [69,70] to describe two-component diffusion in zeolite 4A. In zeolite 4A, the intracage hopping is not a limiting factor ($Đ_{ij} \rightarrow \infty$). The inter-cage hopping is governed by guest–host interactions only, as described by Eq. (47). The Habgood model is thus a special limiting case of the M–S approach.

The mixture sorption characteristics influences mixture diffusion in two ways: (1) mixture sorption determines the magnitudes of the driving forces ($\nabla\theta$), and (2) they contribute to *coupling* of the diffusion process due to the presence of the non-diagonal elements in $[\Gamma]$; even when Eq. (47) applies, the species diffusion is still coupled.

3.3. Verification of M–S formulation for mixture diffusion

Paschek and Krishna [14,30,63,71] carried out KMC simulations for single component, binary and ternary mixture diffusion in MFI zeolite in order to verify the capability of the M–S formulation to predict the Onsager $[L]$ matrix from pure component zero-loading diffusivities $Đ_i(0)$. We present a set of their key results here. Consider a
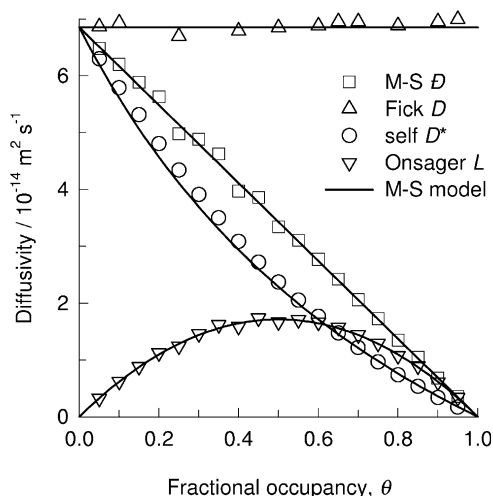
Fig. 15. KMC simulations (open symbols) of M–S, Fick, Onsager and self-diffusivities of 2MH in MFI at 300 K. Data from Paschek and Krishna [30,76]. The continuous lines represent the calculations using Eqs. (19), (20), (24) and (55).

Table 3
Transition probabilities and zero-loading diffusivities for binary mixture in MFI

Species, i	$\Theta_{i,sat}$	v_{zz} (s^{-1})	v_{str} (s^{-1})	$Đ_i(0)$ (m^2 s^{-1})
1 (= 2MH)	4	5×10^4	1.4×10^5	6.85×10^{-14}
2	4	1×10^5	2.8×10^5	13.7×10^{-14}

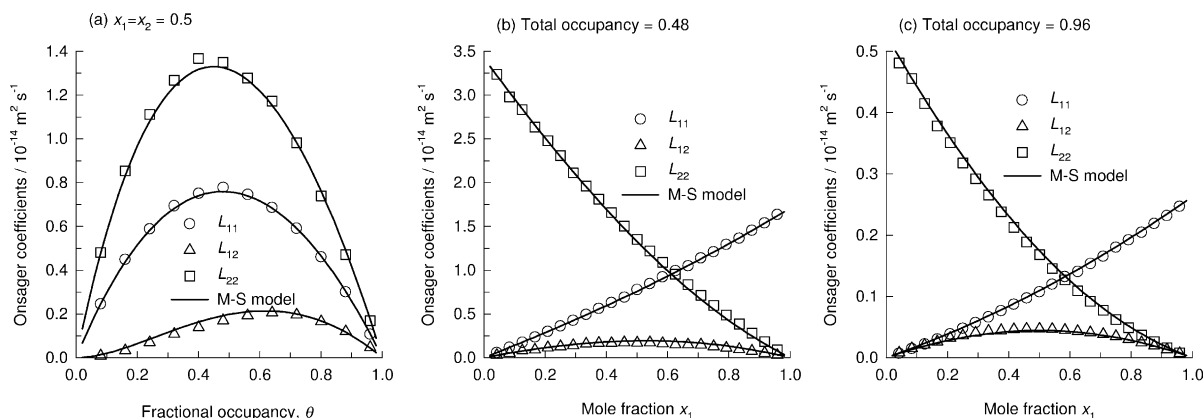Fig. 16. KMC simulations (open symbols) of the Onsager coefficients L_{ij} for binary mixture of component 1 (taken to be 2MH) and 2 in silicalite-1 at 300 K [63]. The jump frequencies are specified in Table 3. The continuous lines are the predictions of the M−S model including finite interchange coefficient $Đ_{ij}$, using Eq. (43).

binary mixture of components 1 and 2, in MFI with the jump frequencies along the straight and zig−zag channels, v_{str} and v_{zz}, as specified in Table 3. For component 1, these frequencies correspond to those of 2-methyl hexane (2MH), calculated from the transition state theory [28]. The jump frequencies for component 2 are taken to be twice the corresponding values for component 1. The zero-loading pure component diffusivities $Đ_i(0)$, calculated using the Kärger formulae given by Eqs. (23) and (24) are also given in Table 3. The saturation loadings of the two components are both taken to be $\Theta = 4$ molecules per unit cell, corresponding to occupation only at the intersection sites.

Consider first the KMC simulations of pure component 2MH. In this case the M−S and Fick diffusivities follow the loading dependences described by Eq. (19) and Eq. (20) respectively; see Fig. 15.

Fig. 16 shows the KMC simulations for the Onsager coefficients L_{ij} in the binary mixture for three cases (a) 50−50 mixture with varying fractional occupancy, (b) for a total occupancy of 0.48 with varying composition of $x_1 \equiv \theta_1/(\theta_1 + \theta_2)$ and (c) for a total occupancy of 0.96 with varying composition of x_1. The KMC simulations show that the cross-coefficient L_{12} has finite, non-zero, values. The assumption of facile exchange, i.e. $Đ_{12} \rightarrow \infty$, is not correct for the MFI topology
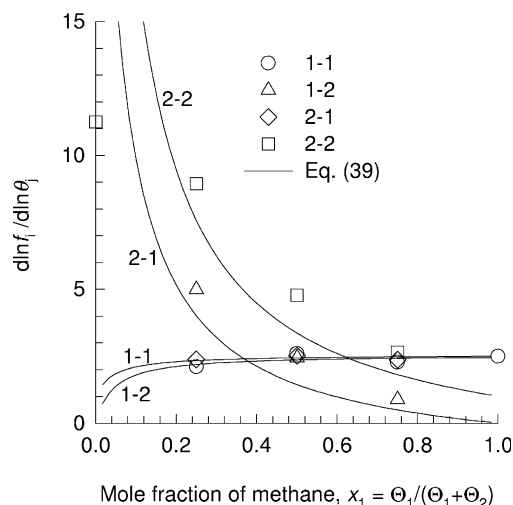

Fig. 17. Comparison of the MD simulated values of $\frac{\partial \ln f_i}{\partial \ln \theta_j}$ with calculations using Eqs. (38 and 39) taking $\Theta_{1,sat} = 10^j$ and $\Theta_{2,sat} = 6.1$ molecules per super cage.

because this would lead to a vanishing value of L_{12} (cf. Eq. (47)). Also shown by continuous lines are the calculations of the Onsager $[L]$ matrix using Eqs. (43) and (44) and Eq. (46). The agreement with the KMC simulation results is excellent, and demonstrates, albeit indirectly, the applicability of the logarithmic interpolation formula Eq. (43) for estimation of the exchange coefficient $Đ_{12}$. It is not possible to directly obtain the $Đ_{12}$ from binary mixture KMC simulations.
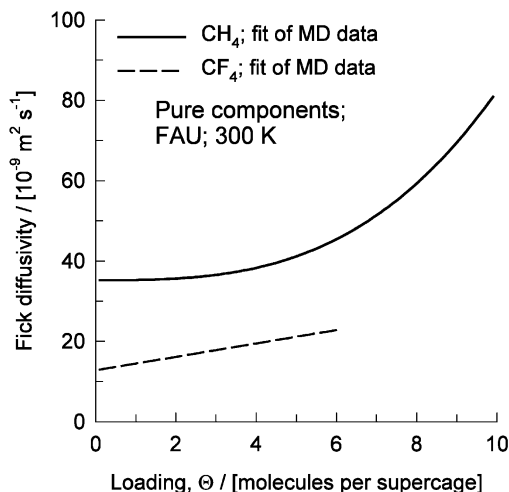
Fig. 18. Pure component Fick diffusivities of CH_4 and CF_4 in FAU at 300 K. The lines are drawn using the fitted parameters given in Table 4 of Sanborn and Snurr [60], representing fits of MD simulations.

In the currently implemented KMC simulations, differences in saturation loadings of individual components are not handled, even though this is not an inherent deficiency. Therefore, it is not possible to test the M–S theory predictions in its ability to capture the influence of unequal saturation capacities. MD simulations do not suffer from this limitation. Sanborn and Snurr [59,60] have performed MD simulations to determine the elements D_{ij} of the Fick matrix [D] for the binary mixture of CH_4 (component 1) and CF_4 (component 2) in Faujasite (FAU) at 300 K. A variety of total mixture loadings $\Theta = 1, 2, 4$ and 6 molecules per supercage were investigated for a range of mixture compositions. Krishna [64] has analysed the MD simulations with a view to test the predictive capability of the M–S theory; here we summarise the main results. The first step in the prediction procedure outlined above is to determine the saturation sorption capacities of CH_4 and CF_4. This information is contained in the MD simulation results for $\frac{\partial \ln f_i}{\partial \ln \theta_j}$ published by Sanborn and Snurr [60]; their data are reproduced by taking the saturation capacities $\Theta_{1,sat} = 10$ and $\Theta_{2,sat} = 6.1$ molecules per supercage respectively for CH_4 and CF_4. The agreement of the MD simulations with the Multicomponent Langmuir calculations

using Eq. (39) of [Γ] is reasonably good [64]; see Fig. 17.

The next step is to determine the M–S diffusivities $Đ_i$ as a function of loading. Sanborn and Snurr report fits of the MD simulations for pure component Fick diffusivities (cf. Table 4 of Ref. [60]); see data plotted in Fig. 18. The Fick diffusivity of CH_4 appears to follow the weak confinement scenario described by Eq. (18). We therefore take the M–S diffusivity for CH_4 to be independent of loading (cf. Eq. (17)) with the value $Đ_1(0) = 35 \times 10^{-9}$ m^2 s^{-1}. The behaviour of CF_4 is more closely in line with the strong confinement scenario of Eq. (20). For CF_4 we take the zero-loading diffusivity $Đ_2(0) = 20 \times 10^{-9}$ m^2 s^{-1} and assume the loading dependence given by Eq. (19). These two distinct behaviours can also be rationalized on the basis of the differences in their molecular sizes.

All the necessary data are now available to estimate the elements of the Fick matrix using Eq. (46). The calculations of D_{11}, D_{12}, D_{21} and D_{22} for a variety of compositions and mixture loadings are presented in Fig. 19 along with the MD simulation results. The predictions of the M–S theory are seen to be in reasonably good agreement with the MD simulations both with respect to the influence of mixture loading Θ (1, 2, 4 and 6) and mixture composition $\Theta_1/(\Theta_1+\Theta_2)$. It is particularly encouraging to note that both the values and composition trends of the cross-terms D_{12} and D_{21} are predicted reasonably well. In order to appreciate the influence of the interchange coefficient $Đ_{ij}$, we consider a limiting case of facile molecule–molecule exchange, i.e. $Đ_{ij} \rightarrow \infty$. The predictions of the Fick matrix [D] for infinite $Đ_{ij}$ are shown in Fig. 20. These predictions are much worse than those witnessed in Fig. 19, with finite $Đ_{ij}$. In particular we note in Fig. 20 that the D_{11} values are much higher than those from MD simulations; signifying that the CH_4 is not being slowed down by CF_4 when we take $Đ_{ij} \rightarrow \infty$. Put another way, the MD simulation results of Sanborn and Snurr [60] point to a significant slowing down of CH_4, concomitant with speeding up of CF_4; these effects can only be accounted for by inclusion of a finite interchange coefficient $Đ_{ij}$.
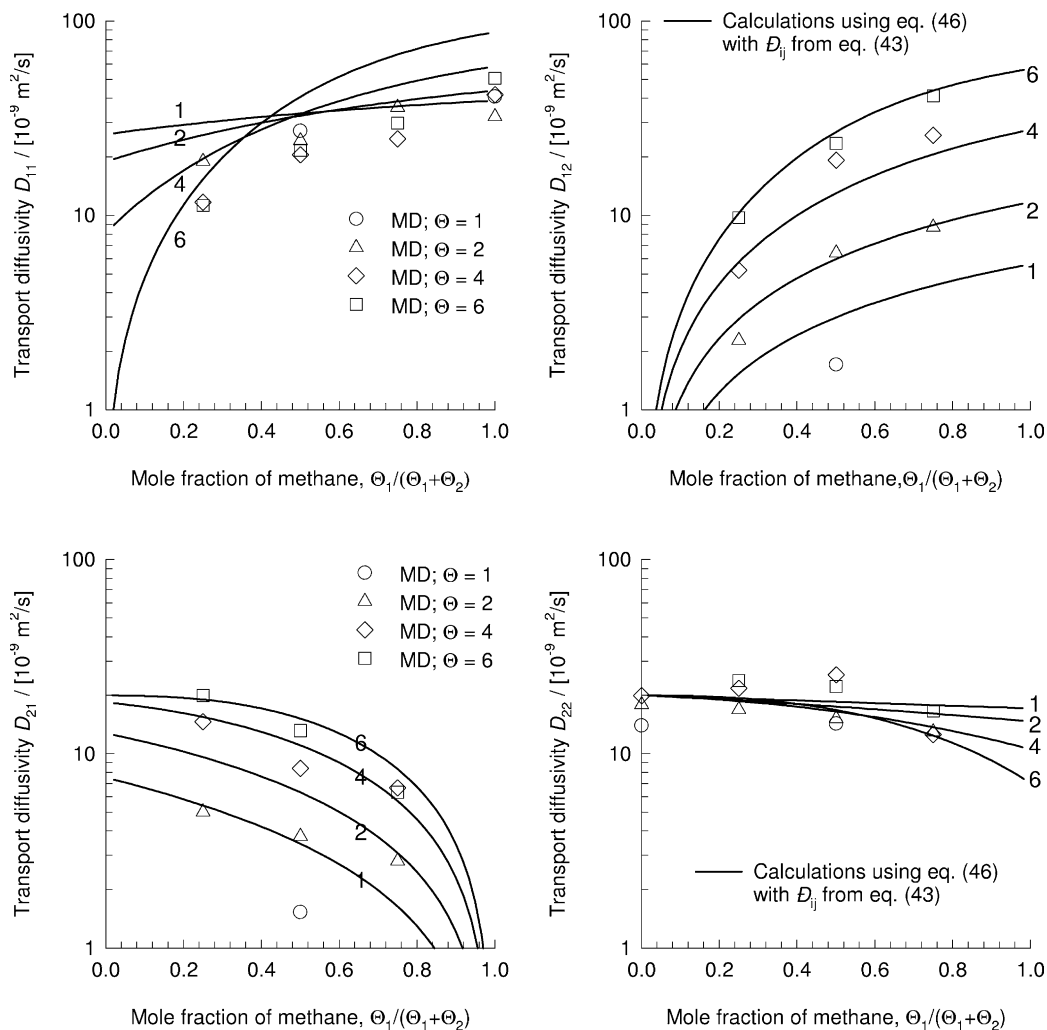
Fig. 19. Comparison of MD simulations of Sanborn and Snurr [60] of the Fick matrix [D] with calculations using Eq. (46). The interchange coefficients are calculated using Eq. (43).

3.4. Self-diffusivities in multicomponent mixtures

Often in practice self-diffusivities are determined in either theory or experiment. Snurr and Kärger [72] performed Pulsed Field Gradient (PFG) NMR measurements and MD simulations to determine self diffusivities in a mixture of CH_4 and CF_4 in MFI zeolite. Jost et al. [73] performed similar studies for mixtures of CH_4 and Xenon in MFI. Gergidis et al. [74,75] studied the self diffusivities in a mixture of CH_4 and n-butane in

MFI using MD and Quasi-elastic Neutron Scattering (QENS). Paschek and Krishna [31,65,76] used KMC simulations to study self diffusivities in various mixtures and in different topologies. Schuring et al. [77] have determined the self-diffusivities in a mixture of n-hexane and 2-methylpentane in MFI using tracer exchange positron emission profiling technique. Self diffusivities in zeolites are more strongly influenced by correlation effects associated with molecular jumps than the Onsager and Fick coefficients.
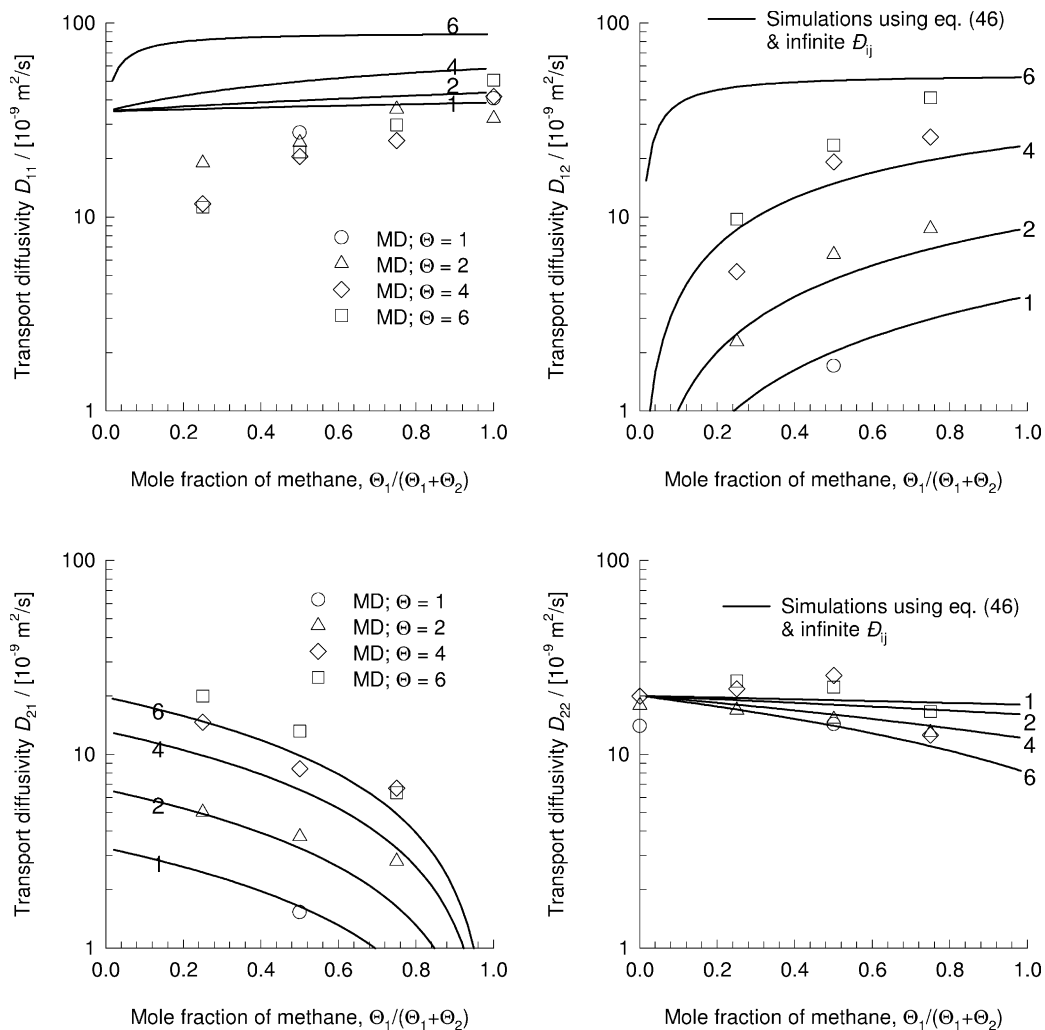
Fig. 20. Comparison of MD simulations of Sanborn and Snurr [60] of the Fick matrix [D] with calculations using Eq. (46), wherein the interchange coefficients are assumed to be infinite.

We shall underline this by first developing a general expression for self-diffusivity of a component in a multicomponent mixture.

Measurements of self-diffusivities are commonly made by labelling (i.e. tracing) species 1 and monitoring it during the diffusion process. Therefore, for determining the self-diffusivity of component 1 in say a ternary mixture consisting of species 1, 2 and 3 we consider a quaternary system made up of species 1, 2, 3 and 4 where species 4 is the labelled species 1. The total number of molecules of 1 and 4 are held constant during

the diffusion process, and therefore we have the constraint:

$$\nabla\theta_4 = \nabla\theta_{1*} = -\nabla\theta_1 \qquad (48)$$

Furthermore, during self-diffusivity measurements of component 1, there are no concentration gradients for species 2 and 3, i.e.

$$\nabla\theta_2 = 0; \quad \nabla\theta_3 = 0 \qquad (49)$$

During tracer diffusion we essentially have equimolar diffusion of component 1 and its labelled form, i.e. component 4, giving:

$$N_1 = -N_4 = -N_{1*} \tag{50}$$

Applying the constraints Eq. (48) and Eq. (49) to Eq. (45) we obtain

$$N_1 = -\rho\Theta_{1,sat}(D_{11} - D_{14})\nabla\theta_1$$
$$= -\rho\Theta_{1,sat}D_1^*\nabla\theta_1 \tag{51}$$

where D_{11} and D_{14} are the (1,1) and (1,4) elements of the Fick matrix $[D]$. Eq. (51) also serves to define the self (or tracer) diffusivity of component 1, D_1^*; this diffusivity is identical to D_{1*}^*, defined by

$$N_4 = N_{1*} = -\rho\Theta_{1,sat}(D_{44} - D_{41})\nabla\theta_4$$
$$= -\rho\Theta_{1,sat}D_{1*}^*\nabla\theta_{1*} \tag{52}$$

because 1 and 4 are the same molecular species. The exchange coefficient $Đ_{14}$ when estimated using Eq. (43) is identical with the pure component M–S diffusivity of component 1, i.e. $Đ_{14} = Đ_{11}$. Furthermore, since species 4 is the tracer component its concentration in the mixture is vanishingly small, i.e. $\theta_4 \to 0$.

Calculating the elements of $[D]$ using Eq. (51), after introducing the various simplifications for tracer diffusion outlined above, we obtain the following simple and elegant expression for D_1^*:

$$D_1^* \equiv D_{11} - D_{14} = \cfrac{1}{\cfrac{1}{Đ_1} + \cfrac{\theta_1}{Đ_{11}} + \cfrac{\theta_2}{Đ_{12}} + \cfrac{\theta_3}{Đ_{13}}} \tag{53}$$

It is clear from Eq. (53) that the self-diffusivity is strongly influenced by particle–particle exchanges $Đ_{12}$ and $Đ_{13}$. Eq. (53) may be extended to a general n-component mixture:

$$D_1^* = \cfrac{1}{\cfrac{1}{Đ_1} + \cfrac{\theta_1}{Đ_{11}} + \cfrac{\theta_2}{Đ_{12}} + \cfrac{\theta_3}{Đ_{13}} + \ldots \cfrac{\theta_n}{Đ_{1n}}} \tag{54}$$

By rotating the subscripts in Eq. (54), analogous expressions are obtained for the self-diffusivities of components $2, 3, \ldots n$. It is important to stress that the expression for the self-diffusivity Eq. (54) is not influenced by the thermodynamic correction factor $[\Gamma]$. Put another way, sorption thermodynamics play no role in the determination of the self-diffusivity.

The expression Eq. (54) reduces for a single component system to

$$D_1^* = \cfrac{1}{\cfrac{1}{Đ_1} + \cfrac{\theta_1}{Đ_{11}}} = \frac{Đ_1}{1 + \theta_1} \tag{55}$$

The calculations of the self-diffusivity of 2MH using Eq. (55), taking $Đ_{11} = Đ_1$, compare very well with the KMC simulation results, as seen in Fig. 15.

For a binary mixture, the formula Eq. (54) simplifies to

$$D_1^* = \cfrac{1}{\cfrac{1}{Đ_1} + \cfrac{\theta_1}{Đ_{11}} + \cfrac{\theta_2}{Đ_{12}}} \tag{56}$$

Consider now the MD simulations of Snurr and Kärger [72] for self diffusvities in a mixture of CH_4 (component 1) and CF_4 (component 2) in MFI zeolite at 200 K. The MD simulations were carried out at a total mixture loading of $\Theta_1 + \Theta_2 = 12$ molecules per unit cell and the methane loading is varied from 0 to 12 molecules per unit cell; their simulation data are shown as open symbols in Fig. 21. We will try to calculate the self diffusivities from pure component data. The pure component diffusivites at zero-loading are estimated as $Đ_1(0) = 60 \times 10^{-10}$, $Đ_2(0) = 25 \times 10^{-10}$ m^2 s^{-1} from the pure component self-diffusivity data of Snurr and Kärger [72]. Methane being a smaller molecule has a higher saturation loading than that of CF$_4$; we therefore take $\Theta_{1,sat} = 22$ and $\Theta_{2,sat} = 13$ on the basis of information on mixture isotherms [78]. The calculations of the diffusivites D_1^* and D_2^* using Eqs. (19) and (43) and Eq. (56) are also shown in Fig. 21(a). The agreement with MD simulations is very good. The dotted lines in Fig. 21(b) represent the calculations of the self-diffusivities, assuming facile exchange, i.e. $Đ_{11} \to \infty$ and $Đ_{12} \to \infty$. The strong influence of correlation effects, embodied in the exchange coefficients, is evident.

(a) With correlation effects, finite exchange   (b) Facile exchange, no correlation effects
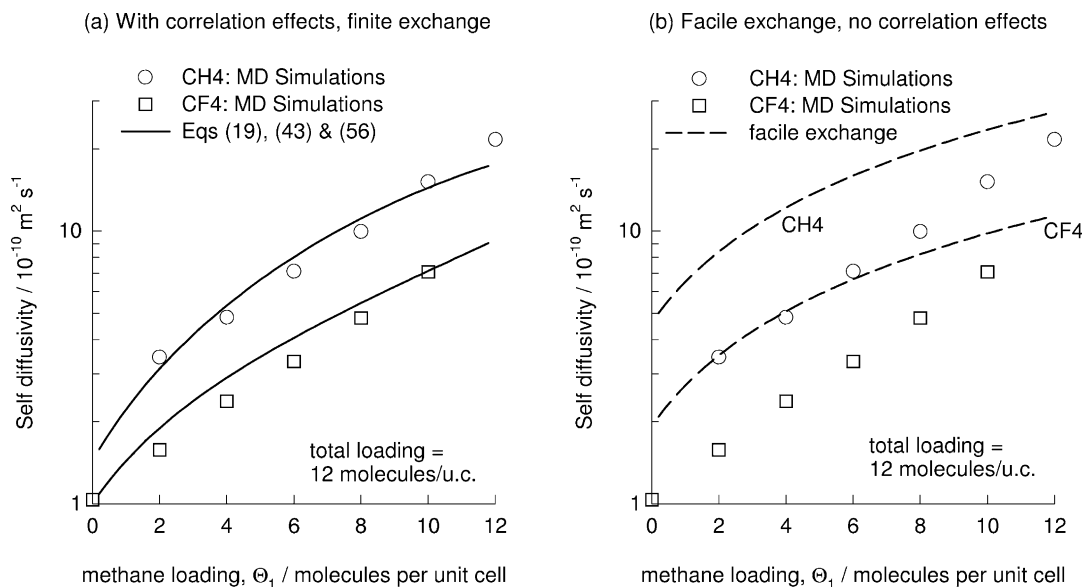

Fig. 21. (a) Comparison of MD binary mixture simulations of Snurr and Kärger [72] for CH_4 and CF_4 in MFI at 200 K with calculations using Eqs. (19), (43) and (56). (b) Calculations of self-diffusivities assuming facile exchange. The calculations were performed taking $Đ_1(0) = 60 \times 10^{-10}$ m^2 s^{-1}, $Đ_2(0) = 25 \times 10^{-10}$ m^2 s^{-1}. The saturation loadings are $\Theta_{1,sat} = 22$ and $\Theta_{1,sat} = 13$ molecules per unit cell.
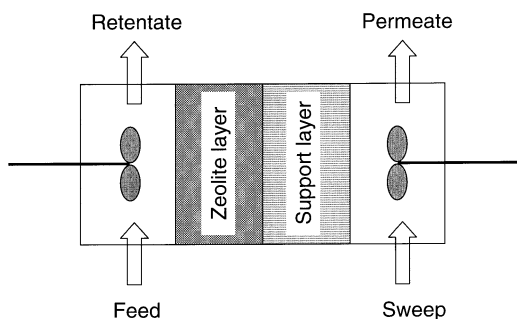

Fig. 22. Schematic of zeolite membrane separation device.

4. Practical examples of zeolite diffusion

Having developed the M−S theory for diffusion, we now consider various practical applications.

4.1. Permeation of single components across zeolite membrane

Zeolite membranes are currently being developed for carrying out separations and catalytic reactions. It is important in practice to determine the permeation fluxes across the membrane. Most commonly, zeolite membrane devices are operated under steady state conditions, though laboratory experiments also monitor the transience prior to achievement of steady state [79–81].

Consider the permeation of a single component, species i, from a well-mixed upstream compartment, across the membrane, to a well-mixed downstream compartment. The permeate gases are often flushed out of the downstream compartment by means of a 'sweep' gas (e.g. helium) in order to maintain the partial pressures of the permeants at low values; see Fig. 22. The zeolite crystals are deposited, or grown, on to a support layer consisting say of metal wool and/or a macroporous layer of sintered stainless steel particles. The diffusion through the support layer is akin to transport through the macropores within a sorbent particle and has been considered in detail by Van de Graaf [80]. The zeolite layer may have nanoscopic defects such as voids and pinholes that can be modelled in the manner described by Nelson et al. [82]. In the following we ignore the support resistance and concentrate on the permeation characteristics of a defect-free zeolite mem-
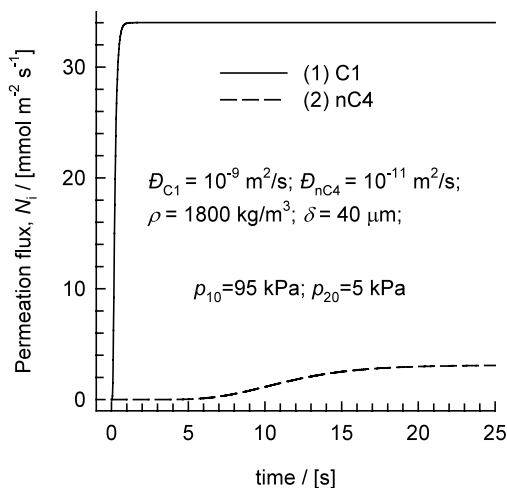
Fig. 23. Single component transient permeation of methane (C1) and n-butane (nC4) across MFI membrane at 300 K.

brane layer (of thickness δ). The reason for our neglect of support resistance is that our objective to highlight several interesting, often peculiar, characteristics of diffusion within the zeolite crystal layer itself; the inclusion of the support layer resistance will change the quantitative results somewhat but not the qualitative features that we wish to stress. The upstream and downstream faces of the zeolite layer are, respectively, in equilibrium with the upstream and downstream partial pressures of the species i:

upstream face:$z = 0$; $p_i = p_{i,0}$; $q_i = q_{i,0}$;

$\Theta_i = \Theta_{i,0}$; $\theta_i = \theta_{i,0}$ (57)

downstream face:$z = \delta$; $p_i = p_{i,\delta}$; $q_i = q_{i,\delta}$;

$\Theta_i = \Theta_{i,\delta}$; $\theta_i = \theta_{i,\delta}$ (58)

The permeation flux is obtained by solving

$$\frac{\partial \theta_i}{\partial t} = -\frac{1}{\rho \Theta_{i,sat}} \frac{\partial N_i}{\partial z} \quad (59)$$

where Eq. (13) is used to describe the single component permeation flux. Details of the numerical techniques employed to solve Eq. (59) are available on our web site: http://ct-cr4.chem.uva.nl/zeolites.

For illustration, let us consider transient permeation of methane (C1) across a MFI membrane at 300 K. The upstream partial pressure of C1 is

held at $p_{1,0} = 95$ kPa. The downstream pressure $p_{i,\delta}$ is maintained at vanishing values by means of a sweep gas. Taking the M–S diffusivity of methane as $Đ_{C1} = 10^{-9}$ m^2 s^{-1}, along with the DSL isotherm parameters reported in Table 1, can be solved to follow the transience in permeation flux N_1 as steady state is approached; the results are shown in Fig. 23. At steady state, the permeation flux of methane is 34 mmol m^{-2} s^{-1}.

The transient permeation of n-butane (nC4) with upstream pressure $p_{2,0} = 5$ kPa is shows a much slower approach to the steady state value of 3.1 mmol m^{-2} s^{-1} (Fig. 23) because of its much lower diffusivity value $Đ_{nC4} = 10^{-11}$ m^2 s^{-1}, and the requirement to achieve a much higher final loading than for C1.

For a binary mixture of C1 (1) and n-C4 (2), with upstream partial pressures of 95 and 5 kPa respectively, we might expect the permeation selectivity, S_P, defined by

$$S_p = \frac{N_2/N_1}{p_{20}/p_{10}} \quad (60)$$

to be $3.1/34.0/(5/95) = 1.73$. We shall demonstrate below this expectation is far removed from reality because of the peculiarities of mixture diffusion in zeolites.

4.2. Permeation of methane–n-butane mixture across MFI membrane

Consider permeation of a 95-5 binary mixture of methane (C1) and n-butane (nC4) across an MFI membrane at 300 K. The first important step in modelling of diffusion is to model the pure component and mixture sorption characteristics; this is required in the determination of the component driving forces $\frac{\partial(\theta)}{\partial r}$ and the thermodynamic correction factor $[\Gamma]$. The pure component isotherms at 300 K in MFI zeolite, obtained from CBMC simulations, are shown in Fig. 6(a), along with the DSL fits using the parameters specified in Table 1. For a 95–5 mixture of C1 and nC4, the component loadings in the mixture obtained from CBMC simulations are shown in Fig. 24(a). The x-axis in Fig. 24(a) strictly refers to
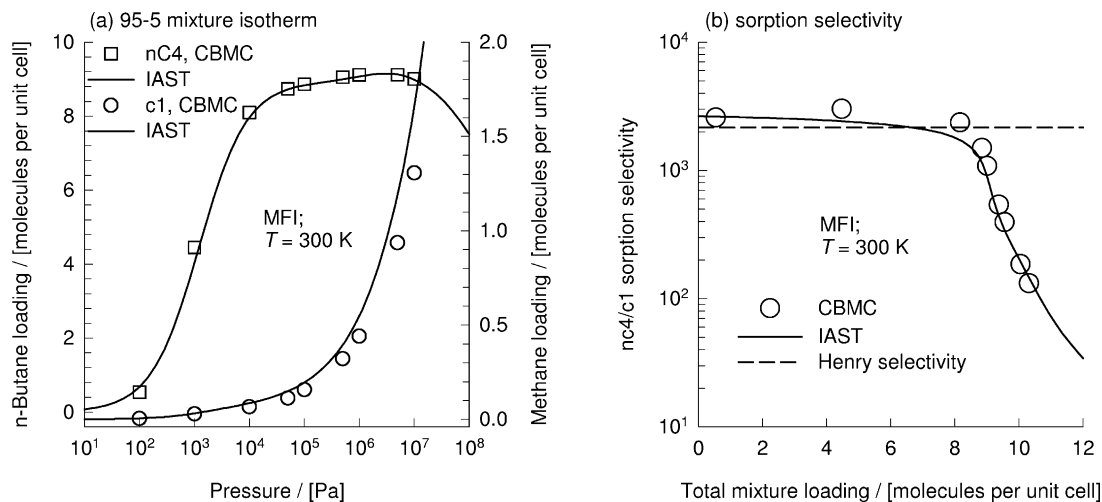
Fig. 24. (b) Sorption loadings of 95–5 binary mixture of C_1 and nC_4 in MFI at 300 K. (b) nC_4/C_1 sorption selectivity. The continuous lines represent the predictions of the IAST.

the component fugacities, as these are the quantities that are obtained from CBMC simulations. The loading of C1 increases monotonically with increasing pressure. On the other hand the loading of nC_4 reaches a plateau value for pressures in the 1–5 MPa range. Increasing the total systems pressure beyond 5 MPa, leads to a decline in the loading of nC_4! In Fig. 24(b) we plot the sorption selectivity, S, defined by:

$$S = \frac{\Theta_2/\Theta_1}{p_2/p_1} \qquad (61)$$

where p_1 and p_2 are the partial pressures in the bulk gas phase. For mixture loadings, $\Theta_{mix} = \Theta_1 + \Theta_2$, below 8, the sorption selectivity of nC_4 with respect to C1 is practically constant and equals that calculated from the corresponding Henry coefficients, i.e. 2200. However, as Θ_{mix} increases beyond 8, the sorption selectivity decreases dramatically to values about one to two order of magnitude lower. Near saturation loadings, the vacant spaces in the zeolite are more easily occupied by the smaller methane molecule. This is a size entropy effect that favours smaller sized molecules. It is clear that the size entropy effects counter the usual effect of chain length; increase in the chain length favours the adsorption of the larger sized molecule.

From a practical point of view it is important to be able to predict the mixture isotherms from pure component isotherm data. It is clear that the multicomponent Langmuir isotherm will be totally unsuccessful in this regard because the sorption selectivity predicted by this model will be independent of the mixture loading. Let us try to estimate the mixture loadings from the pure component isotherms using the Ideal Adsorbed Solution theory (IAST) of Myers and Prausnitz [83]. Briefly, the basic equation of IAST theory is the analogue of Raoult's law for vapour–liquid equilibrium, i.e.

$$Py_1 = P_i^0(\pi)x_i; \quad i = 1, 2, \ldots n \qquad (62)$$

where x_i is the mole fraction in the adsorbed phase

$$x_i = \frac{\Theta_i}{\Theta_1 + \Theta_2 + \ldots \Theta_n} \qquad (63)$$

and $P_i^0(\pi)$ is the pressure for sorption of every pure component i, which yields the same surface potential, ϕ_i^0, expressed in $(J\,m^{-3})$, for the pure components, as that for the mixture, ϕ:

$$\frac{\phi_1^0}{k_B T} = \frac{\phi}{k_B T} = \rho \int_{P=0}^{P=P_i^0} \frac{\Theta_i^0(P)}{P} dP \qquad (64)$$

where k_B is the Boltzmann constant, ρ is the density of MFI expressed in terms of the number
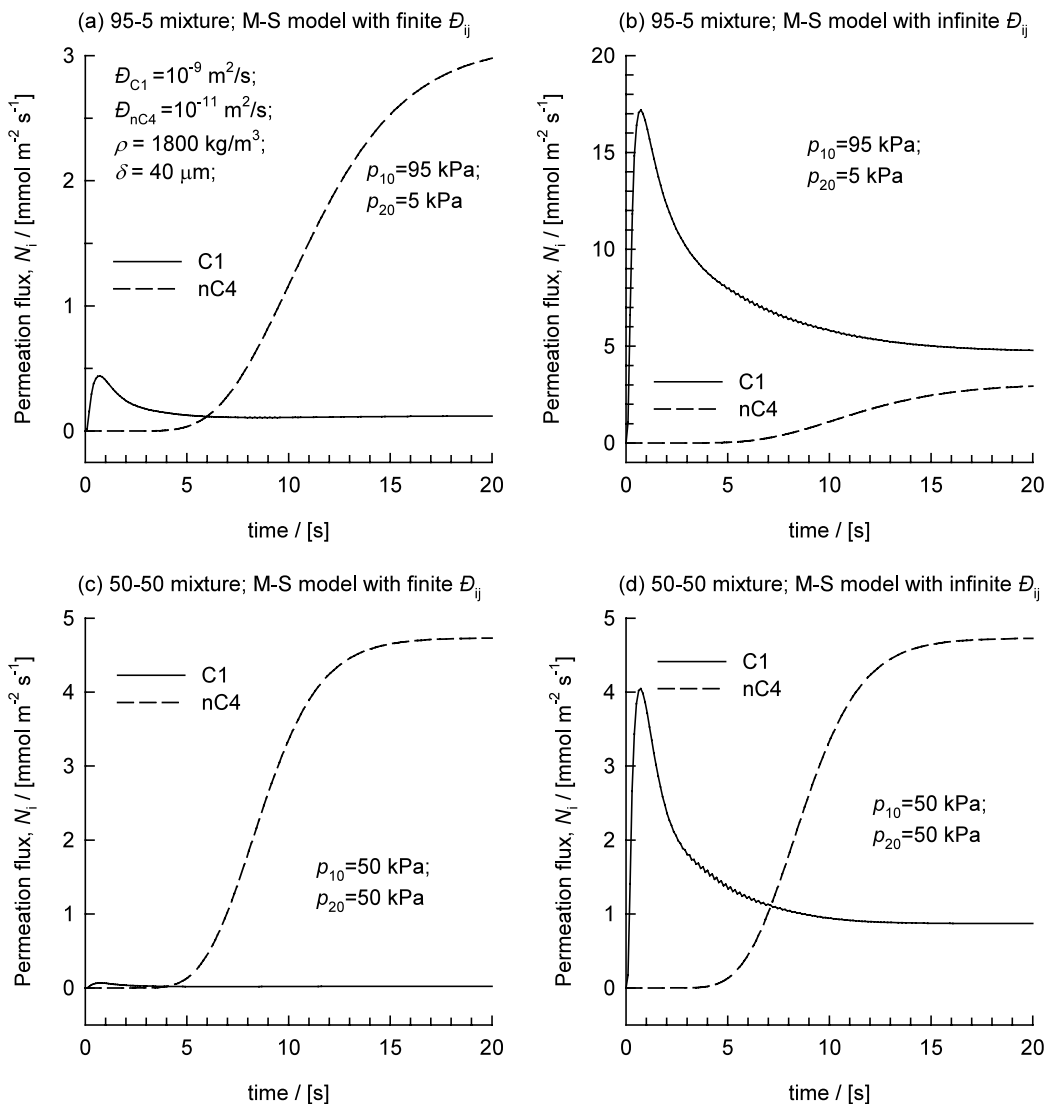
(a) 95-5 mixture; M-S model with finite $Đ_{ij}$

$Đ_{C1} = 10^{-9}$ m²/s;
$Đ_{nC4} = 10^{-11}$ m²/s;
$\rho = 1800$ kg/m³;
$\delta = 40$ μm;

$p_{10} = 95$ kPa;
$p_{20} = 5$ kPa

C1
nC4

(b) 95-5 mixture; M-S model with infinite $Đ_{ij}$

$p_{10} = 95$ kPa;
$p_{20} = 5$ kPa

C1
nC4

(c) 50-50 mixture; M-S model with finite $Đ_{ij}$

C1
nC4

$p_{10} = 50$ kPa;
$p_{20} = 50$ kPa

(d) 50-50 mixture; M-S model with infinite $Đ_{ij}$

C1
nC4

$p_{10} = 50$ kPa;
$p_{20} = 50$ kPa

Fig. 25. (a and b) Transient permeation across MFI membrane of 95–5 mixture of C_1 and nC_4 in MFI at 300 K. (c and d) Transient permeation of 50–50 mixture of C_1 and nC_4 in MFI at 300 K. Two implementations of the M–S model are compared, with finite and infinite interchange coefficients $Đ_{ij}$.

of unit cells per m³ and $\Theta_i^0(P)$ is the pure component isotherm given by Eq. (32). The total amount adsorbed is obtained from

$$\Theta_{mix} \equiv \Theta_1 + \Theta_2 + \cdots + \Theta_n$$

$$= \frac{1}{\dfrac{x_1}{\Theta_1^0(P_1^0)} + \dfrac{x_2}{\Theta_2^0(P_2^0)} + \cdots + \dfrac{x_n}{\Theta_n^0(P_n^0)}} \quad (65)$$

The set of Eqs. (32), (62)–(64) and Eq. (65) need to be solved numerically to obtain the loadings of the individual components in the mixture. We see in Fig. 24(a and b) that the IAST predictions are in excellent agreement with the CBMC simulation results. Size entropy effects are properly accounted for in the IAST mixture model. In this review we deal primarily with mixtures of alkanes and the IAST mixture model is successful; this conclusion

is however not general and the reader is referred to Sircar [84] who shows that the IAST can break down when the adsorbate sizes and the degree of adsorbent heterogeneity for adsorption of the components differ substantially.

Now let us consider permeation of the C1 (1)–nC4 (2) mixture across a MFI membrane for a situation with upstream partial pressures $p_{1,0} = 95$ kPa, $p_{2,0} = 5$ kPa. The downstream partial pressures $p_{i,\delta}$ are assumed to be maintained at vanishing values by means of a sweep gas. The boundary conditions, Eq. (57) and Eq. (58), are thus determined. The set of differential Eq. (59) are solved together with the (coupled) flux M–S relations Eq. (45) in order to obtain the fluxes N_i across the membrane. The results are shown in Fig. 25 (a). The steady state fluxes of C1 and nC4 are found, respectively, to be 0.12 and 3.09 mmol m^{-2} s^{-1} giving a nC4/C1 permeation selectivity value (Eq. (60)), $S_P = 487$. In Section 3.1 we have calculated the permeation selectivity on the basis of pure component permeation to be 1.73. Mixture permeation selectivities cannot be predicted on the basis of pure component permeation data.

During the initial transience, the methane flux attains a maximum in the flux (with a value of 0.44

mmol m^{-2} s^{-1}) at $t = 0.73$ s. The reason for this peak is that during the initial period, methane that has a diffusivity value 100 times that of nC4 diffuses faster through the membrane. However as time progresses and the MFI structure gets increasingly occupied with nC4 that dislodges the less-strongly adsorbed C1. The flux of nC4 is enhanced with increased nC4 loading. Concomitantly, the flux of C1 decreases due to the fact that the loading in the MFI decreases. Furthermore, in the M–S model the interchange coefficient $Đ_{ij}$ serves to slow down methane and speed up nC4. All these factors leads to a decline in the flux of C1 from its peak value of 0.44 to the steady state value of 0.12 mmol m^{-2} s^{-1}.

The predictions of the fluxes with the M–S model assuming $Đ_{ij} \rightarrow \infty$ and using Eq. (47) are shown in Fig. 25(b). There is no slowing down of methane due to interchange and therefore the initial transience shows a peak methane flux of 17.2 mmol m^{-2} s^{-1}, that reduces at steady state to 4.72. The steady state flux of nC4 is 3.06 mmol m^{-2} s^{-1} and the permeation selectivity is calculated as $S_P = 12.3$, significantly lower than the value of 487 using the complete M–S theory with finite interchange. The experimental value of S_P for this 95−5 mixture determined by Bakker [79] is 380, quite close to the estimations of the M–S model including interchange.

A similar picture emerges for permeation of a 50−50 mixture; see Fig. 25(c and d). The respective values of the permeation selectivities are $S_P = 202$ and 5.4. The experimental value of S_P for this 50−50 mixture determined by Bakker [79] is 60. Clearly, the interchange process within MFI matrix occurs at a finite rate.

We carried out a series of simulations with varying mixture compositions in the upstream membrane compartment, keeping the total upstream pressure at 100 kPa; the calculations of S_P with the M–S model, both with finite interchange, following Eq. (43), and taking $Đ_{ij} \rightarrow \infty$, are shown in Fig. 26, along with the Bakker experimental data [79]. The decrease in the permeation selectivity with increasing partial pressure of nC4 is essentially a size entropy effect that comes into play at high occupancies and favours the smaller methane molecule. If we had used the multi-
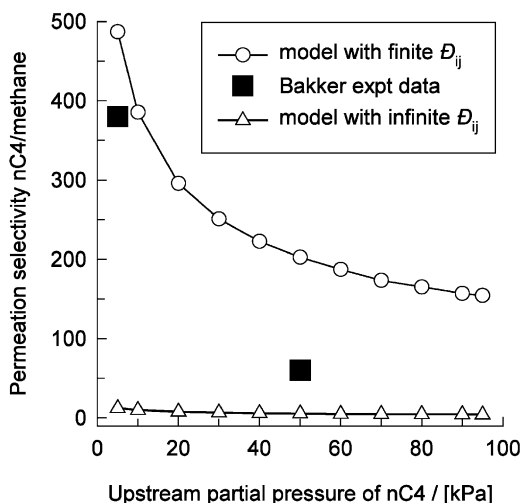

Fig. 26. Dependence of nC$_4$/C$_1$ permeation selectivity on the two implementations of M–S model, with and without inclusion of the interchange coefficient $Đ_{ij}$. Also shown are the experimental data of Bakker [79].
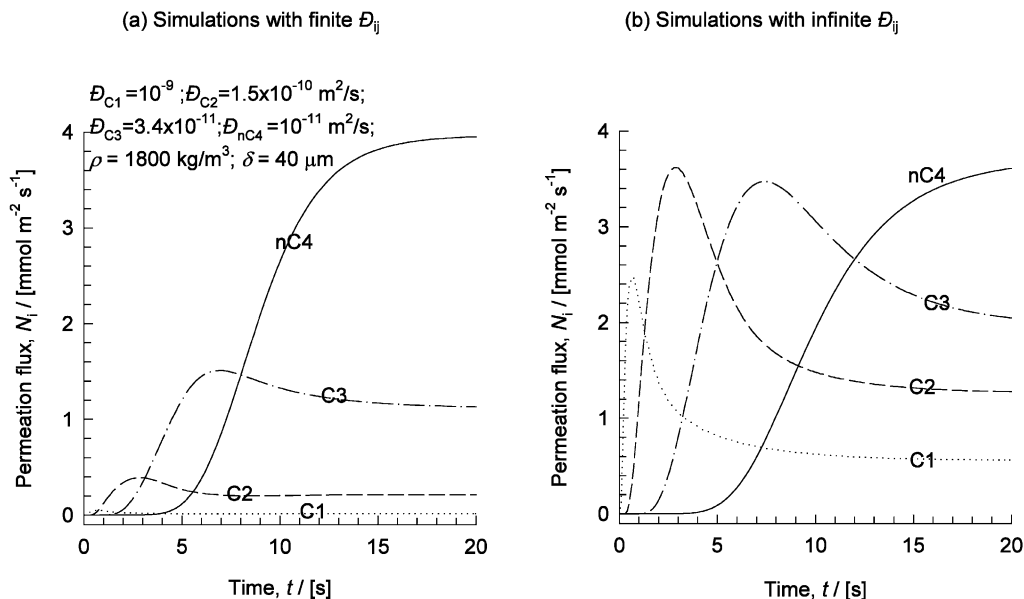
Fig. 27. Permeation fluxes for an equimolar quaternary mixture of C_1, C_2, C_3, and nC_4 across an MFI zeolite membrane at 300 K. The isotherm data is specified in Table 1. The M–S diffusivities are taken from the thesis of van de Graaf [80]. The permeation selectivities are calculated using two implementations of M–S model, (a) with and (b) without inclusion of the interchange coefficient $Đ_{ij}$. Animations of the transient permeations can be viewed by logging on to our website: http://www.ct-cr4.chem.uva.nl/zeolites.

component Langmuir isotherm, taking the saturation capacities of C1 and $nC4$ to be equal to one another, the S_P would be predicted to be independent of the upstream composition and have a constant value of 800.

The transient fluxes during permeation of an equimolar quaternary mixture of C1, C2, C3 and $nC4$ across a MFI membrane, with upstream partial pressures $p_{i,0} = 25$ kPa are shown in Fig. 27(a); the calculations here include finite $Đ_{ij}$ from Eq. (43). It is interesting to note that the permeation of C1 is virtually suppressed in the presence of the more strongly adsorbing C2, C3 and $nC4$. The corresponding simulation results with infinite $Đ_{ij}$ are shown in Fig. 27(b). Noteworthy are the high peaks in the permeation of C1, C2 and C3 during the initial transience. Also, the $nC4/C3$, $C3/C2$, $C2/C1$ permeation selectivities are significantly lower than for the case with finite $Đ_{ij}$.

Kapteijn et al. [12] and Krishna and Paschek [13] have analyzed permeation data for C1-C2 and C1-C3 mixtures across a MFI membrane to stress the need for recognizing the size entropy effects (with the use of the IAST model) and the

importance of including finite interchange coefficients $Đ_{ij}$ in the M–S formulation.

4.3. Permeation of hexane isomers across MFI zeolite membrane

The separation of mixtures of isomers of alkanes in the 5–7 C atom range is an important activity in the petroleum and petrochemical industries. For example, the products from a catalytic isomerization reactor consist of a mixture of linear, mono-methyl and di-methyl alkanes. Of these, the di-branched molecules are the most desired ingredients in petrol because they have the highest octane number. It is therefore required to separate the di-methyl alkanes and recycle the linear and mono-methyl alkanes back to the isomerization reactor [85]. In the detergent industry, the linear alkanes are the desired components and need to be separated from the alkane mixture. We examine below the specific case of separation of hexane isomers using MFI zeolite membrane permeation.

Consider first the separation of nC_6 and 3MP. We first need to understand the pure component
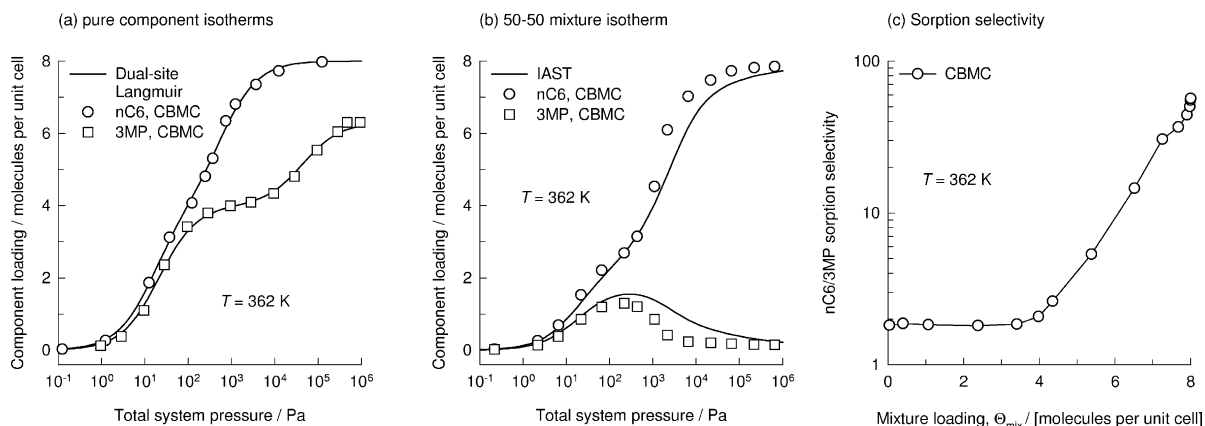
Fig. 28. (a) Pure component isotherms for nC_6 and 3MP in MFI at 362 K. CBMC calculations and DSL fits. (b) Component loadings for 50–50 mixture obtained from CBMC simulations compared with IAST predictions. (c) nC_6/3MP sorption selectivity as function of the total mixture loading Θ_{mix}.

and mixture sorption behaviours. The pure component isotherms of hexane isomers nC_6 and 3MP into MFI zeolite at 362 K, obtained from CBMC simulations, are shown in Fig. 28(a). The loadings in a 50–50 mixture are shown in Fig. 28(b). For $\Theta_{mix} < 4$ the isomers have practically the same sorption strength. However, the loading of the mono-branched isomer reduces to very low values when $\Theta_{mix} > 4$. The reason for this 'exclusion' of the 3MP is because of configurational entropy effects that tend to favour the linear isomer. For $\Theta_{mix} < 4$, the 3MP molecules prefer to locate at the intersections between the straight channels and zig–zag channels [13,39,40]. The normal alkane can be located anywhere within the MFI matrix. At $\Theta_{mix} = 4$, all the intersection sites are fully occupied. The 3MP demands an extra 'push' to locate within the channel interiors (witness the inflection in the pure component isotherms in Fig. 28(a)). 3MP suffers a penalty from configurational entropy considerations because these molecules 'pack' less efficiently within the MFI matrix; this penalty causes 3MP to be virtually excluded from the MFI matrix near saturation loadings $\Theta_{mix} = 8$. The sorption selectivity, S, defined by Eq. (61), is plotted in Fig. 28(c) as a function of the total mixture loading; S increases significantly above unity values when the mixture loading Θ_{mix} exceeds 4 molecules per unit cell.

Also shown in Fig. 28(b) are the IAST calculations of the component loadings with the DSL

parameters reported in Table 2; these are in reasonably good agreement with the CBMC simulation results; it appears that the IAST mixture rule properly accounts for configurational entropy effects. Clearly, such effects are not accounted for by the multicomponent Langmuir model to predict mixture isotherms. In an earlier publication [13] we had shown that for more accurate estimates of the mixture isotherm, we may need to use the Real Adsorbed Solution Theory (RAST).

The mixture results shown in Fig. 28 are of practical importance because they provide a means of separating the hexane isomers in a membrane permeation device, relying on configurational entropy effects. The key is to operate at conditions such that the mixture loading at the upstream face of the membrane corresponds to $\Theta_{mix} > 4$; at 362 K this corresponds to a total upstream pressure in excess of 1 kPa. We shall illustrate this by considering permeation of an equimolar mixture of nC_6 and 3MP across an MFI zeolite membrane, keeping the upstream compartments at a total pressure of 66 kPa. We take the zero-loading M–S diffusivity of nC_6 to be five times that of 3MP, following Cavalcante and Ruthven [86]. The transient permeation fluxes, calculated using the M–S model including finite $Đ_{ij}$, are shown in Fig. 29(a). The steady state permeation selectivity S_P can be calculated to be 43.2. Simulations were carried out for a range of system pressures in the
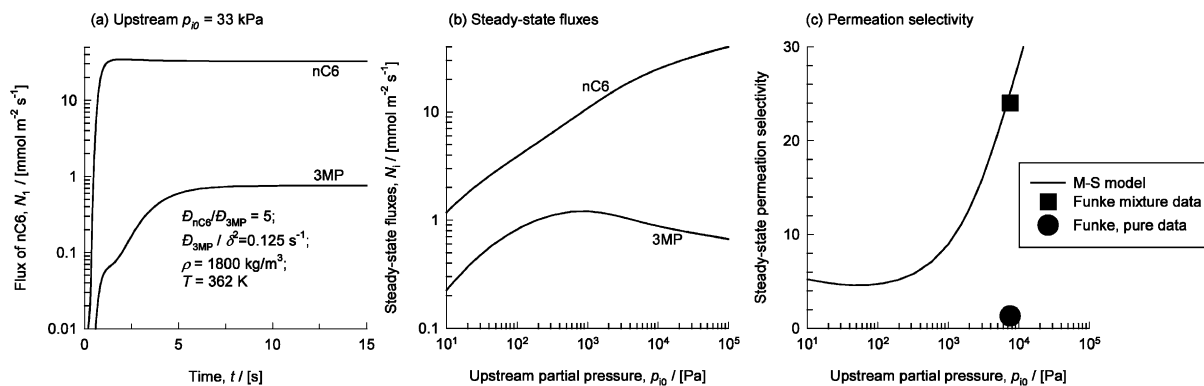
Fig. 29. (a) Transient diffusion fluxes for permeation of 50–50 mixture of nC_6 and 3MP across MFI membrane at 362 K. The upstream partial pressures are $p_{i0} = 33$ kPa. (b) Steady state permeation fluxes as a function of upstream hydrocarbons pressure. (c) Separation selectivities as function of upstream hydrocarbons pressure. The experimental data points in (c) are from Funke et al. [87]. The isotherm parameters are given in Table 2. The M–S model takes account of finite interchange coefficient $Ð_{ij}$, using Eq. (43). The Maxwell–Stefan diffusivities of the isomers are $Ð_{nC6} = 5Ð_{3MP}$ and the membrane thickness is chosen such that $Ð_{3MP}/\delta^2 = 0.125$ s^{-1}.

upstream compartment; the results for the fluxes and selectivity are shown in Fig. 29(b) and (c) respectively. We note that values of S_P in excess of 10 can be obtained when the pressure in the upstream compartment increases beyond 2 kPa; the results in Fig. 29(c) mirror the sorption selectivity results shown in Fig. 28(c). For operation with an upstream pressure of 15 kPa, Funke et al. [87] have experimentally determined a value S_P of 24; this is in good agreement with our simulation results; see the large filled square in Fig. 29(c). More important is the observation of Funke

et al. [87] that the permeation selectivity based on pure components was found to be only 1.3; see the large filled circle in Fig. 29(c). This underlines the fact that subtle configurational entropy effects are at play here.

The same entropy principle can be used to separate nC_6 and 2,2DMB, as has been demonstrated by Gump et al. [88], and underpinned using CBMC simulations [13,45,89].

In practice, it is more difficult to separate the mono-branched 3MP from the di-branched isomer 2,2DMB. Simulations of the transient and steady

Fig. 30. (a) Transient diffusion fluxes for permeation of 50–50 mixture of 3MP and 2,2DMB across MFI membrane at 362 K. The upstream partial pressures are $p_{i0} = 33$ kPa. (b) Steady state permeation fluxes as a function of upstream hydrocarbons pressure. (c) Separation selectivities as function of upstream hydrocarbons pressure. The isotherm parameters are given in Table 2. The M–S model takes account of finite interchange coefficient $Ð_{ij}$, using Eq. (43). The Maxwell–Stefan diffusivities of the isomers are $Ð_{3MP} = 2Ð_{2,2DMB}$ and the membrane thickness is chosen such that $Ð_{3MP}/\delta^2 = 0.125$ s^{-1}.
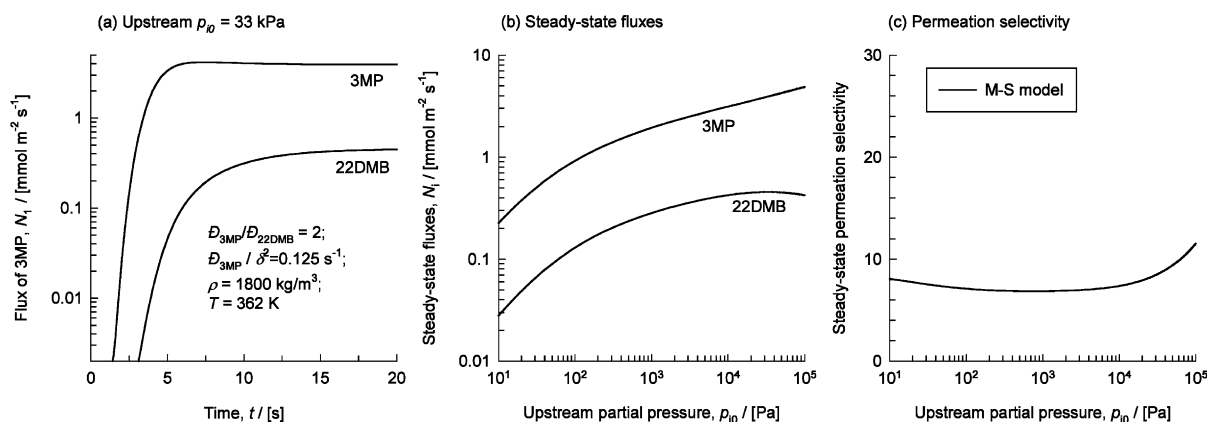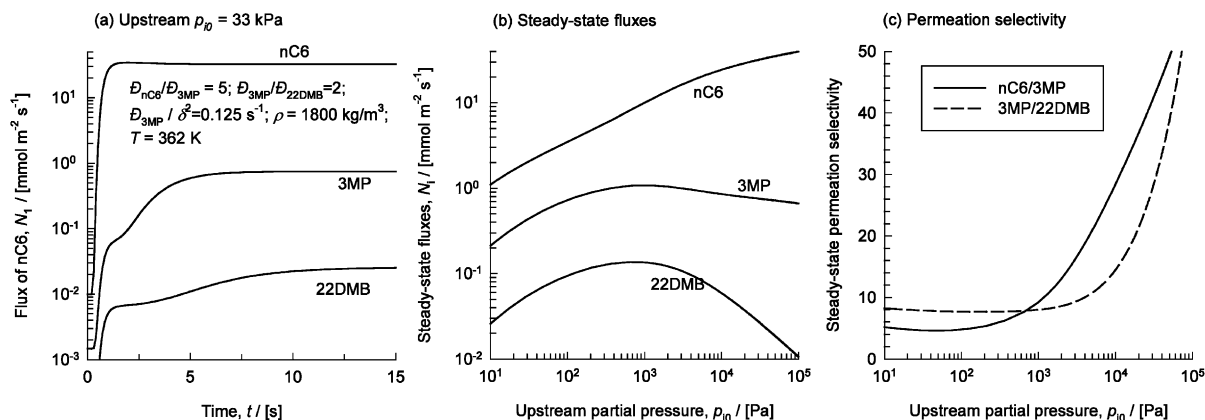
Fig. 31. (a) Transient diffusion fluxes for permeation of equimolar mixture of nC_6, 3MP and 2,2DMB across MFI membrane at 362 K. The upstream partial pressures are $p_{i0} = 33$ kPa. (b) Steady state permeation fluxes as a function of upstream hydrocarbons pressure. (c) Separation selectivities as function of upstream hydrocarbons pressure. The Maxwell–Stefan diffusivities of the isomers are $Đ_{nC6} = Đ_{3MP} = 10Đ_{2,2DMB}$. The M–S model takes account of finite interchange coefficient $Đ_{ij}$, using Eq. (43).

Table 4

Pure component Langmuir parameters and M–S diffusivities for N_2 and CH_4 in 4A zeolite at 193.7 K

	N_2	CH_4
Saturation loading q_{sat} (mol kg^{-1})	3.75	3.86
Langmuir parameter, b (Pa^{-1})	1.08×10^{-4}	2.56×10^{-4}
$Đ_i$ (m^2 s^{-1})	3.9×10^{-18}	1.8×10^{-19}
Crystallite radius, r_c (m)	0.5×10^{-6}	0.5×10^{-6}

Data from Habgood [69].

state fluxes, along with the permeation selectivities are shown in Fig. 30. In these simulations we use the isotherm data as given in Table 2, based on CBMC simulations [13,43,45,89], and use IAST to predict mixture isotherms. The experimental results of Funke et al. [87] confirm the much lower selectivities for 3MP/2,2DMB separation as compared to nC_6/3MP separation.

One way to improve the 3MP/2,2DMB selectivity is to allow this mixture to permeate in the presence of nC_6; simulations of permeation of an equimolar *ternary* mixture are presented in Fig. 31. The higher sorption strength of nC_6, especially at higher partial pressures, ensures that the mixture loading Θ_{mix} exceeds 4 molecules per unit cell, thereby resulting in high nC_6/3MP and 3MP/2,2DMB selectivities; see Fig. 31(c). For example when the upstream partial pressures are 30 kPa,

3MP/2,2DMB selectivities in excess of 30 are obtained with ternary mixture permeation; this is significantly higher than the value of 7 obtained by binary mixture permeation; see Fig. 30(c).

4.4. Uptake of N_2 and CH_4 in zeolite 4A crystallite

Consider uptake of N_2 and CH_4 into a spherical zeolite 4A crystal at 193.7 K. Experimental data for pure component sorption parameters and diffusivities have been published in the classic paper by Habgood [69]; these data have been reported in Table 4. The pure component characteristics are interesting because while CH_4 has a higher sorption strength (witness the higher Langmuir b parameter in Table 4), its diffusivity is considerably lower. The uptake characteristics into 4A zeolite from a bulk vapour mixture maintaining $p_{N2} = 50.9$ kPa and $p_{CH_4} = 49.1$ kPa are shown in Fig. 32. The Habgood data (open symbols) show that N_2 exhibits a peak during its transience to equilibrium. The reason for this is clear; starting with (virgin) zeolite, the initial loadings are dominated by the faster diffusing N_2. As time progresses, the slower diffusing but more strongly adsorbing CH_4 displaces N_2.

Using the pure component data in Table 4, simulations for the uptake were carried out with the M–S model, both with finite interchange
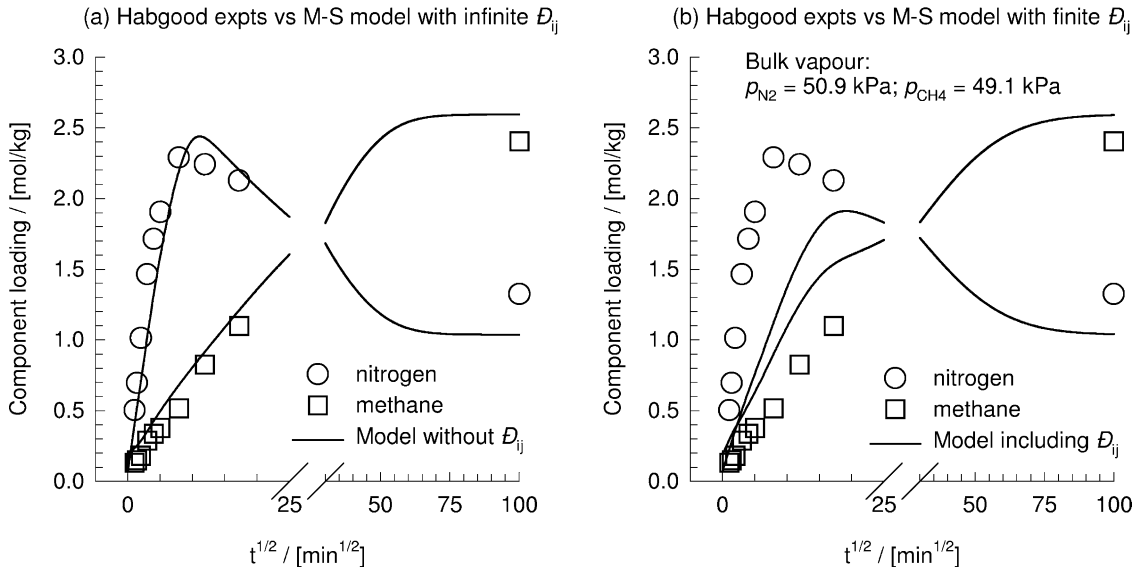
(a) Habgood expts vs M-S model with infinite $Ð_{ij}$

(b) Habgood expts vs M-S model with finite $Ð_{ij}$

Bulk vapour:
$p_{N2} = 50.9$ kPa; $p_{CH4} = 49.1$ kPa

nitrogen
methane
Model without $Ð_{ij}$

nitrogen
methane
Model including $Ð_{ij}$

$t^{1/2}$ / [min$^{1/2}$]

$t^{1/2}$ / [min$^{1/2}$]

Component loading / [mol/kg]

Fig. 32. Transient uptake of 50.9% N_2, 49.1% CH_4 mixture into spherical crystallite of 4A zeolite at 193.7 K. Experimental data of Habgood [69]. Two implementations of the M–S model are compared, with finite and infinite interchange coefficient $Ð_{ij}$. The model parameters are given in Table 4.

coefficient $Ð_{ij}$ calculated using Eq. (43) (Fig. 32(b)) and taking $Ð_{ij} \rightarrow \infty$ (Fig. 32(a)). Both M–S model approaches predict a peak in the N_2 flux, but the model assuming $Ð_{ij} \rightarrow \infty$ does a much better job of quantitatively predicting the uptake profiles. Hab-

good has also published experimental data for uptake into 4A zeolite from a bulk vapour mixture maintaining $p_{N_2} = 10$ kPa and $p_{CH_4} = 90$ kPa; these data are shown in Fig. 33, along with the two implementations of the M–S model. Again we

(a) Habgood expts vs M-S model with infinite $Ð_{ij}$

(b) Habgood expts vs M-S model with finite $Ð_{ij}$

nitrogen
methane
Model without $Ð_{ij}$

Bulk vapour:
$p_{N2} = 10$ kPa;
$p_{CH4} = 90$ kPa

nitrogen
methane
Model including $Ð_{ij}$

$t^{1/2}$ / [min$^{1/2}$]

$t^{1/2}$ / [min$^{1/2}$]
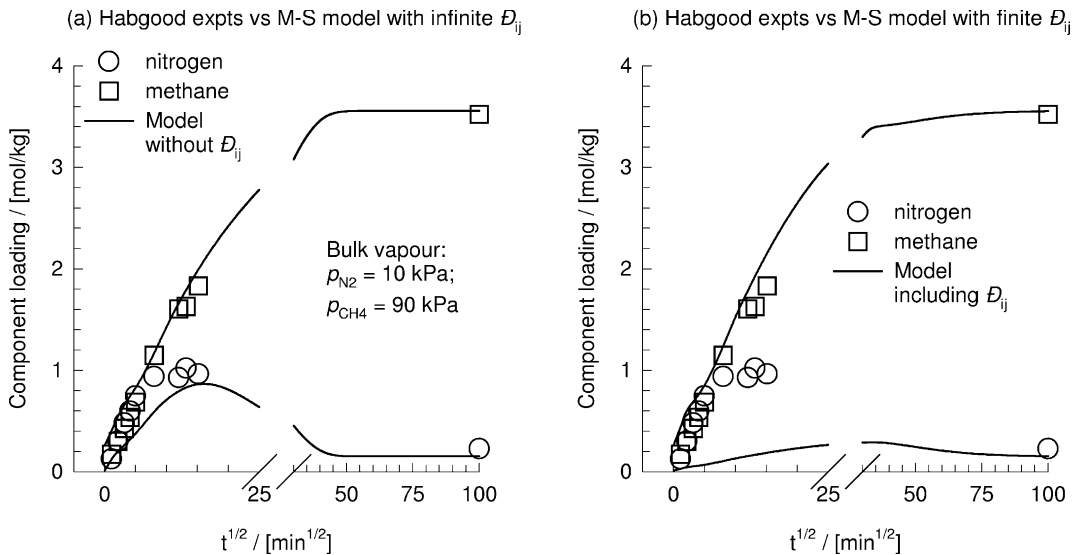
Component loading / [mol/kg]

Fig. 33. Transient uptake of 10% N_2, 90% CH_4 mixture into spherical crystallite of 4A zeolite at 193.7 K. Experimental data of Habgood [69]. Two implementations of the M–S model are compared, with finite and infinite interchange coefficient $Ð_{ij}$. The model parameters are given in Table 4.
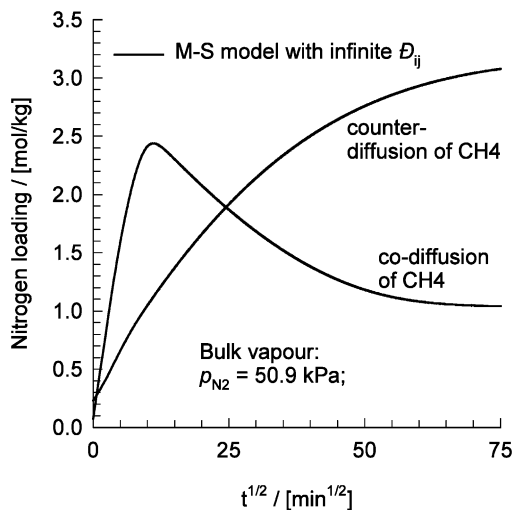
Fig. 34. Transient uptake of N_2 into spherical crystallite of 4A zeolite at 193.7 K. Comparison of uptakes for co- and counter-diffusion of CH_4. The M−S model calculations assumes $Đ_{ij} \rightarrow \infty$. The model parameters are given in Table 4.

note that that M−S model, assuming $Đ_{ij} \rightarrow \infty$ does a very good job of predicting the mixture diffusion behaviour. It appears that diffusion of N_2 and CH_4 in the zeolite 4A follows the behaviour described by Eq. (47) and is essentially free from vacancy correlation effects.

In the transient uptake shown in Fig. 32 we had co-diffusion of N_2 and CH_4 within 4A zeolite. Let us focus on the transient uptake of N_2 and compare two situations: (1) with co-diffusion of CH_4, and (2) with CH_4 diffusing in a direction counter-current to N_2. The counter-current scenario is achieved by pre-equilibrating the zeolite with CH4 exposing it to a bulk vapour with $p_{CH_4} = 49.1$ kPa. This pre-equilibrated zeolite is then exposed to a bulk vapour with $p_{N_2} = 50.9$ kPa. Simulations using the M−S model, taking $Đ_{ij} \rightarrow \infty$, are compared in Fig. 34. The two uptake characteristics are markedly different. During co-diffusion, N_2 and CH_4 compete for sorption sites because they move in the same 'direction'; N_2 wins in the early stages, yields the majority of the sorption sites to CH_4 eventually. There is no competition during counter-diffusion but there is co-operation, CH_4 diffuses out and makes way for the incoming N_2.

The asymmetry in co- and counter- diffusion has also been verified in experimental studies [90].

4.5. Chromatographic separation of O_2 and N_2 using 4A zeolite

The separation of O_2 from N_2, can be achieved by exploiting the differences in their diffusivities in small pore 4A zeolite. The separation process is commonly carried out in a packed bed of sorbent particles (Fig. 35). We now develop a model for breakthrough in this packed bed for the case in which intra-crystalline diffusion is the controlling resistance and the macropore/mesopore diffusion resistance is ignored. The reason for ignoring the macropore/mesopore resistance is that we wish to illustrate the many interesting, and peculiar features of intra-zeolite diffusion. Assuming plug flow, the concentration at any position and instant of time obtained by solving the following set of partial differential equations (details can be found in Refs. [2,4,6,7,91–94])

$$\frac{\partial c_i}{\partial t} = -\frac{\partial(uc_i)}{\partial z} - \left(\frac{1-\varepsilon}{\varepsilon}\right)\rho\frac{\partial \bar{q}_i}{\partial t} \qquad (66)$$

where c_i is the molar concentration in the gas phase, u is the fluid phase (absolute) velocity, z is the axial coordinate distance, ε is the bed porosity, ρ is the density of the zeolite crystals and $\bar{q}_i$ is the average concentration within the spherical particle given by Eq. (29). Details of the numerical techniques employed to solve Eq. (66) are available on our web site: http://www.ct-cr4.chem.uva.nl/zeolites/. In chromatographic separations, two types of feed injection strategies are employed: step and pulse injection. Usually the LDF approximation is made in order to avoid solving the intra-particle diffusion numerically. Furthermore, published models for breakthrough in packed beds [2,4,6,7] almost invariably use the multicomponent Langmuir isotherm to describe mixture diffusion. Use of either LDF or the multicomponent Langmuir isotherm is not to be recommended in the general case where subtle entropy effects come into play, affecting sorption and diffusion. For accurate modelling, therefore, there is no avoiding the
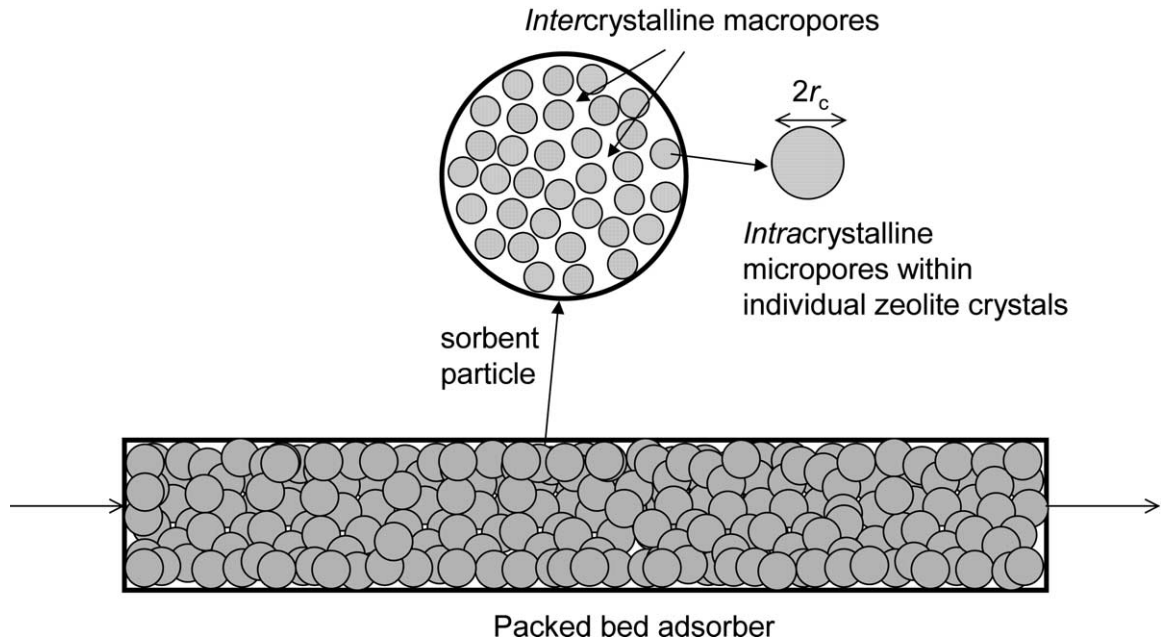
Intercrystalline macropores

$2r_c$

Intracrystalline
micropores within
individual zeolite crystals

sorbent
particle

Packed bed adsorber

Fig. 35. Schematic of adsorbed packed with zeolite particles.

Table 5
Pure component Langmuir parameters and M–S diffusivities for O_2 and N_2 in 4A zeolite at 298 K

	O_2	N_2
Saturation loading q_{sat} (mol kg^{-1})	15.61	10.46
Langmuir parameter, b (Pa^{-1})	4.95×10^{-8}	1.43×10^{-7}
$Đ_i$ (m^2 s^{-1})	1.438×10^{-14}	1.519×10^{-16}
Partial pressures at inlet to packed bed p (kPa)	63.8	240.2
Packed bed voidage, ε (–)	0.4	0.4
Length of bed, L (m)	0.6	0.6
Interstitial gas velocity at inlet to bed, u_0 (m s^{-1})	0.0436	0.0436
Crystallite radius, r_c (nm)	1300, 650 or 130	1300, 650 or 130

Data from Farooq and Ruthven [93] and Haas et al. [91]. Also given are the parameters of the packed bed.

use of the IAST and using a rigorous solution of intra-crystalline diffusion.

Consider the breakthrough behaviour for air (21% O_2, 79% N_2) at a pressure of 300 kPa in a packed bed of 0.6 m length; other details and parameters are specified in Table 5. As is conven-

tional, we plot the normalized concentrations of the two components at the exit, as a function of the dimensionless time $\tau \equiv \dfrac{tu_0}{L}$ where u_0 is the interstitial gas velocity at the inlet to the packed bed. First we consider the step injection strategy. In Fig. 36(a) the breakthrough curves with the M–S model (with infinite interchange coefficient $Đ_{ij}$) are shown for the case where the crystallite particle radius r_c is chosen to be 1300 nm. This choice of r_c ensures that there is strong intracrystalline diffusion limitation. During the initial breakthrough pure N_2 exits the adsorber. The slower-diffusing N_2 exhibits a 'rollup' whereas O_2 does not; a rollup is said to occur if the transient molar concentration in the gas phase exceeds the inlet value, i.e. $c_i/c_{i0} > 1$. When the crystallite particle radius r_c is chosen to be 650 nm, both N_2 and O_2 are found to exhibit rollup behaviours; see Fig. 36(b). Again we note that pure N_2 can be separated from the mixture at the outlet during the initial transience. The breakthrough behaviours change dramatically when the crystallite particle radius r_c is reduced to 130 nm; see Fig. 36(c). In this case, the breakthrough behaviour is uninfluenced by intracrystal-
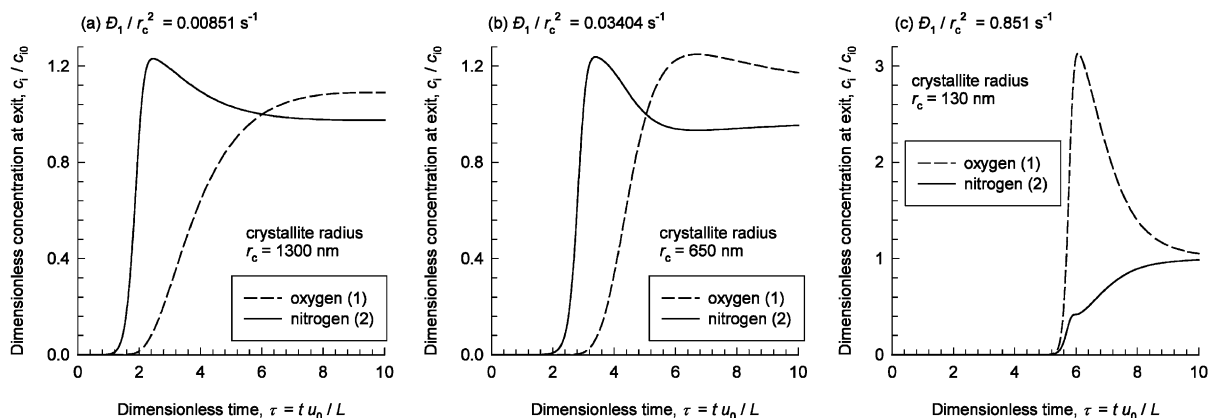
Fig. 36. Breakthrough (response to step change) of N_2 and O_2 through packed bed of 4A zeolite particles for three different particle sizes. Adsorber data specified in Table 5.

line diffusion and is dictated by the adsorption equilibrium characteristics. The less-strongly adsorbed O_2 displays pronounced rollup behaviour whereas, N_2 does not. It is clear from Fig. 36 that if we wish to collect pure N_2 as product, we should use crystallite sizes in the 650–1300 nm range, and operate under conditions of intracrystalline diffusion control.

The response to pulse injection (duration of 1 s) of air, is shown in Fig. 37. Again we note that for crystallite sizes of 1300 and 650 nm, N_2 breaks through in almost pure form during the initial transience, i.e. $\tau < 1$. For a particle size of 130 nm, nearly pure N_2 can be recovered in the *latter* stages of the breakthrough, for $\tau > 7$.

There is evidence in the Refs. [4,94], that a proper model of multicomponent mixture diffusion is essential for the success of this technology for air separation.

4.6. Chromatographic separation of C5 and C6 alkanes using MFI zeolite

Jolimaitre et al. [95] have reported experimental breakthrough curves for binary and ternary mixtures containing 2-methylbutane (2MB), 2-methyl-petane (2MP) and 2,2dimethylbutane (2,2DMB) obtained in bed packed with MFI crystals at a temperature of 473 K. We have simulated their results, ignoring macropore diffusion resistances;
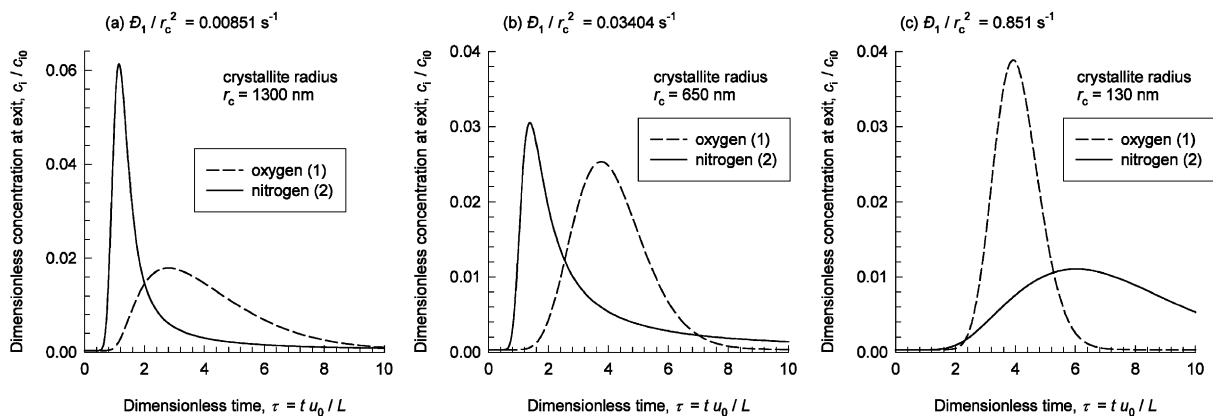

Fig. 37. Breakthrough of N_2 and O_2 through packed bed of 4A zeolite particles for three different particle sizes for pulse input (1 s duration). Adsorber data specified in Table 5.

Table 6
Pure component Langmuir parameters and M–S diffusivities for 2MB, 2MP and 2,2DMB in MFI zeolite at 473 K

	2MB	2MP	2,2DMB
Saturation loading q_{sat} (mol kg^{-1})	4	4	4
Langmuir parameter, b (Pa^{-1})	4.12×10^{-5}	1.27×10^{-4}	7.12×10^{-5}
M–S diffusivity of pure components, $Đ_i$ (m^2 s^{-1})	3×10^{-14}	2×10^{-14}	2.5×10^{-16}
Length of bed, L (m)	0.795	0.795	0.795
Crystallite radius, r_c (nm)	200	200	200
	Extrudates I	Extrudates II	
Packed bed voidage, ε (−)	0.33	0.4	
Crystal density ρ (kg m^{-3} of packed bed)	650.8	620.8	

Data from Jolimaitre et al. [95]. Also given are the parameters of the packed bed.

the key input data are summarized in Table 6; other data can be found in their paper [95]. Firstly, let us consider the simulations of the break-throughs of the three binary pairs, Runs 12, 14 and 17 of Jolimaitre et al. [95]. The continuous curves shown in Fig. 38 represent the calculations using the M–S model, taking account of finite interchange coefficient $Đ_{ij}$, using Eq. (43). The agreement between model and experimental data is reasonably good, and remarkable when we consider that only pure component data have been used in the simulations. A similar good agreement is obtained when we compare the experimental breakthroughs with the ternary mixture of 2MB–2MP–2,2DMB (Runs 21 and Run 22) with the M–S model calculations; see Fig. 39.

4.7. Chromatographic separation of hexane isomers using MFI zeolite

One of the important problems facing the petroleum industry is the separation of the isomers of hexane into three fractions consisting of the linear, mono-branched, and di-branched isomers. We now demonstrate that this is possible by considering an equimolar mixture of nC_6, 3MP and 2,2DMB and separating it in pulsed chroma-tographic operation at 362 K using an adsorber packed with MFI crystals. The isotherm para-meters are given in Table 2. In order to ensure good separation it is important initially to preload the zeolites so that the mixture loading is main-tained at a loading higher than 4 molecules per
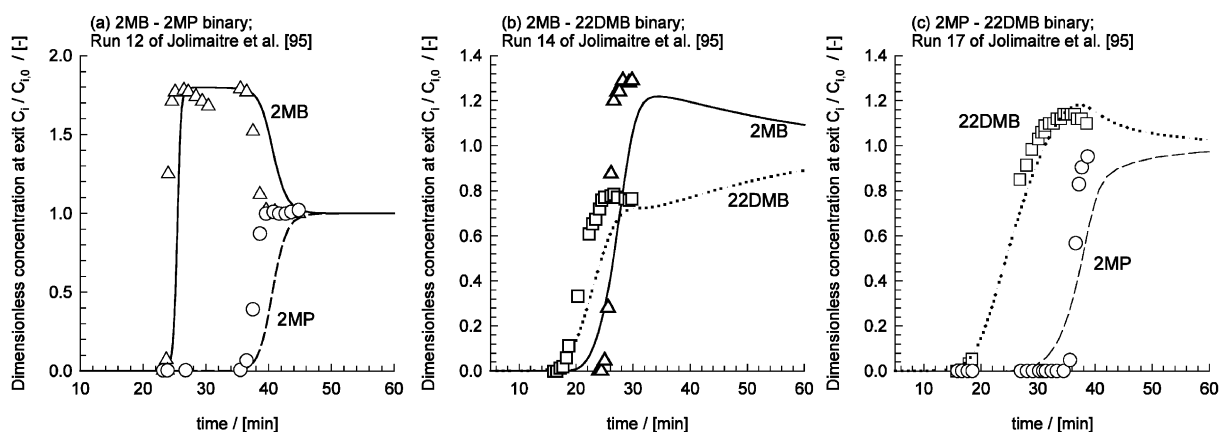

Fig. 38. Breakthrough curves measured by Jolimaitre et al. [95] for (a) Run 12 with 2MB–2MP binary mixture, (b) Run 14 with 2MB–2,2DMB binary mixture, and (c) Run 17 with 2MP–2,2DMB binary mixture. The continuous lines are the predictions of the M–S model implementation, taking account of finite interchange coefficient $Đ_{ij}$, using Eq. (43). Input data are as specified in Table 6. Animations of the breakthrough can be viewed by logging on to our website: http://ct-cr4.chem.uva.nl/zeolites.
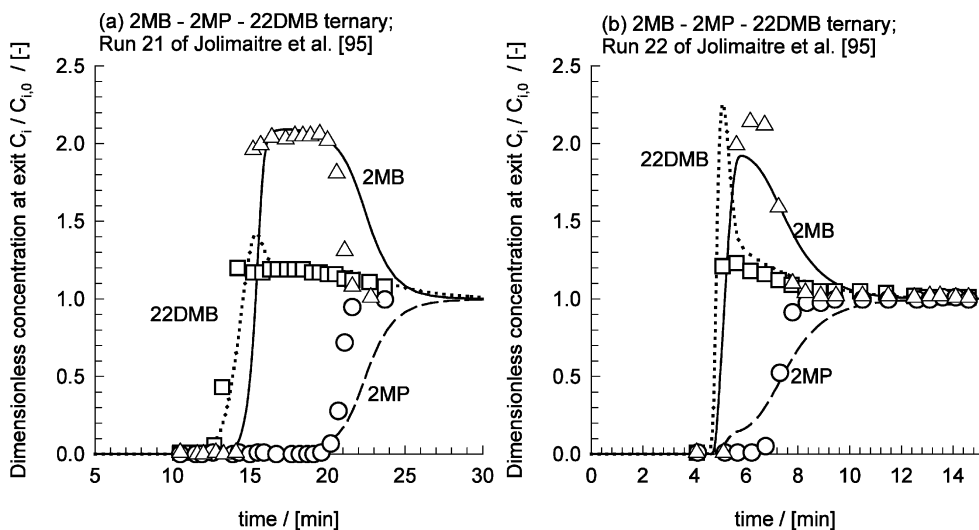
Fig. 39. Breakthrough curves measured by Jolimaitre et al. [95] for (a) Run 21 and (b) Run 22 with a ternary mixture 2MB–2MP–2,2DMB. The continuous lines are the predictions of the M–S model implementation, taking account of finite interchange coefficient $Đ_{ij}$, using Eq. (43). Input data are as specified in Table 6.
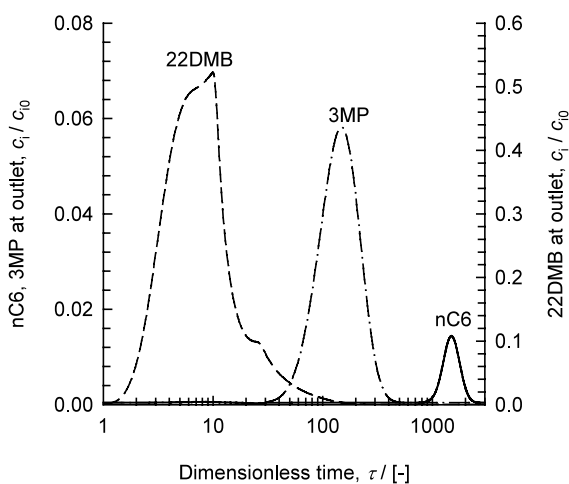

Fig. 40. Breakthrough of a mixture of hexane isomers nC_6, 3MP and 2,2DMB, swept by nC_5, in a pulsed chromatograph packed with MFI crystals. The temperature $T = 362$ K; the porosity of the packed bed $\varepsilon = 0.4$; length of packed bed $L = 0.2$ m; interstitial gas velocity at inlet $u_0 = 0.07240$ m s^{-1}; density of MFI $\rho = 1800$ kg m^{-3}. The Maxwell–Stefan diffusivities of the isomers are $Đ_{nC6} = 5Đ_{3MP} = 10Đ_{2,2DMB} = Đ_{nC5}/5$. The radius of the crystallites r_c was chosen such that $Đ_{2,2DMB}/r_c^2 = 0.001$ s^{-1}. Animations of the breakthrough can be viewed by logging on to our website: http://www.ct-cr4.chem.uva.nl/zeolites.

unit cell. This is done by initially bringing the bed to equilibrium with a mixture of n-pentane ($nC5$, the sweep component) at partial pressure of 36 kPa, and the three hexane isomers nC_6, 3MP and 2,2DMB each at a partial pressure of 5 kPa. Fig. 40 shows the breakthrough obtained when a pulse consisting of a mixture of nC_6, 3MP and 2,2DMB, at partial pressures of 12 kPa each, is injected through the chromatograph for a period of 25 s. After 25 s, the bed is swept with nearly pure $nC5$ (that plays the role of desorbent) maintained at a partial pressure of 36 kPa. The MFI crystallite size is chosen such that $Đ_{2,2DMB}/r_c^2 = 0.001$ s^{-1}. The other M–S diffusivites are taken as $Đ_{nC6}/Đ_{3MP} = 5$; $Đ_{3MP}/Đ_{2,2DMP} = 2$; $Đ_{nC5}/Đ_{nC6} = 5$. We note that 2,2DMB is first eluted from the bed, followed by 3MP and, $nC6$ is the last to exit the bed. This is the separation that is desirable in practice, because the linear and mono-branched isomers can then be recycled back to the catalytic isomerization reactor [85].

Pulsed chromatography may therefore be used to separate di-branched from the mono-branched isomers of hexane.

5. Conclusions

The proper description of mixture sorption and diffusion is essential in applications of zeolites for separation and reaction. In this review we have focussed on intra-crystalline diffusion process. The following major points and conclusions emerge from the foregoing discussions.

1) Intra-crystalline diffusion and sorption processes are inter-twined; proper models are required to describe both phenomena.
2) Adsorption and desorption of single components proceed at significantly different rates.
3) The sorption isotherm of some type of molecules e.g. branched alkanes in MFI, show inflection; this inflection behaviour has a significant impact on the mixture sorption and diffusion.
4) For mixtures of molecules that differ in their saturation loadings, the proper description of the mixture isotherm requires the use of the IAST; the multicomponent Langmuir isotherm is inadequate in this case. In an earlier publication [13] we had shown that for more accurate estimates of the mixture isotherm, we may need to use the RAST. Differences in the saturation loadings leads to a size entropy effect that favours sorption of the smaller molecule.
5) The size entropy effect can have a significant impact on the membrane permeation selectivity.
6) For sorption of mixtures of linear and branched alkanes in MFI, configurational entropy effects come into play; this causes the branched alkanes to be virtually excluded from the zeolite. Configurational entropy effects can be exploited for achieving separations of alkane isomers.
7) The M–S approach allows the prediction of the mixture diffusion on the basis of information on the pure component M–S diffusivities, $Đ_i$, along with the mixture isotherms (estimated using say the IAST). The interchange coefficient $Đ_{ij}$ accounts for the slowing-down of the molecule with the higher mobility, along with the speeding-up of the molecule with the lower mobility.
8) In MFI zeolite, the complete M–S model, with a finite interchange coefficient $Đ_{ij}$ is required for proper description of mixture diffusion. This has been verified both from KMC simulations and by comparison with experimental data on membrane permeation.
9) Published experimental data of Habgood [69] for uptake of N_2 and CH_4 in zeolite 4A are better simulated by the M–S model in which the interchange occurs at an infinite rate, i.e. $Đ_{ij} \rightarrow \infty$. There is a need for carrying out further MD and KMC simulations, with a variety of mixtures in various zeolite topologies, in order to obtain guidelines for deciding a priori, when we need to use finite interchange coefficients $Đ_{ij}$ and for which cases the approximation i.e. $Đ_{ij} \rightarrow \infty$ will be adequate.
10) There is a need for more experimental data on mixture diffusion in various zeolite structures in order to gain a better understanding of the influence of guest topology on the mixture diffusion characteristics.
11) Co- and counter-diffusion of binary mixtures are asymmetric phenomena.
12) Accurate prediction of breakthrough behaviour in a packed bed requires proper modelling of intra-crystalline mixture diffusion. LDF modelling approaches are inadequate when intra-crystalline diffusion is the predominant controlling resistance. When macropore/micropore resistances become important, LDF approximations may be adequate.
13) The illustrative examples in Section 4 show that it is possible to exploit configurational entropy effects in developing novel processes for separating di-branched alkanes from mono-branched alkanes; such separations are of great importance in the petroleum industry.

One major shortcoming of the treatment in this paper is the neglect of the thermal effects caused by heats of adsorption. Temperature gradients inside zeolite particles need to be taken into

account for a proper quantitative modelling of instationary processes such as pressure swing adsorption beds.

Acknowledgements

References

[1] R.M. Barrer, Zeolites and Clay Minerals as Sorbents and Molecular Sieves, Academic Press, London, 1978.

[2] D.M. Ruthven, Principles of Adsorption and Adsorption Processes, Wiley, New York, 1984.

[3] J. Kärger, D.M. Ruthven, Diffusion in Zeolites and Other Microporous Solids, Wiley, New York, 1992.

[4] D.M. Ruthven, S. Farooq, K.S. Knaebel, Pressure Swing Adsorption, VCH Publishers, New York, 1994.

[5] D.M. Ruthven, M.F.M. Post, Diffusion in zeolite molecular sieves, in: H. van Bekkum, E.M. Flanigan, P.A. Jacobs, J.C. Jansen (Eds.), Introduction to Zeolite Science and Practice, Second edition (Chapter 12), Elsevier, Amsterdam, 2001 (Chapter 12).

[6] R.T. Yang, Gas Separation by Adsorption Processes, Butterworth, Boston, 1987.

[7] D.D. Do, Adsorption Analysis: Equilibria and Kinetics, Imperial College Press, London, 1998.

[8] N.Y. Chen, T.F. Degnan, C.M. Smith, Molecular Transport and Reaction in Zeolites. Design and Application of Shape Selective Catalysts, VCH Publishers, New York, 1994.

[9] R. Krishna, Multicomponent surface-diffusion of adsorbed species-a description based on the generalized Maxwell–Stefan equations, Chem. Eng. Sci. 45 (1990) 1779–1791.

[10] R. Krishna, Problems and pitfalls in the use of the Fick formulation for intraparticle diffusion, Chem. Eng. Sci. 48 (1993) 845–861.

[11] R. Krishna, J.A. Wesselingh, The Maxwell–Stefan approach to mass transfer, Chem. Eng. Sci. 52 (1997) 861–911.

[12] F. Kapteijn, J.A. Moulijn, R. Krishna, The generalized Maxwell–Stefan model for diffusion in zeolites: sorbate molecules with different saturation loadings, Chem. Eng. Sci. 55 (2000) 2923–2930.

[13] R. Krishna, D. Paschek, Separation of hydrocarbon mixtures using zeolite membranes: a modelling approach combining molecular simulations with the Maxwell–Stefan theory, Sep. Purif. Technol. 21 (2000) 111–136.

[14] R. Krishna, D. Paschek, Verification of the Maxwell–Stefan theory for diffusion of three-component mixtures in zeolites, Chem. Eng. J. 87 (2002) 1–9.

[15] A. Einstein, Investigations on the Theory of Brownian Movement, Dover, New York, 1956.

[16] J.A. Wesselingh, R. Krishna, Mass Transfer in Multicomponent Mixtures, Delft University Press, Delft, 2000.

[17] R. Krishna, A unified approach to the modelling of intraparticle diffusion in adsorption processes, Gas Sep. Purif. 7 (1993) 91–104.

[18] A.I. Skoulidas, D.S. Sholl, Direct tests of the Darken approximation for molecular diffusion in zeolites using equilibrium molecular dynamics, J. Phys. Chem. B 105 (2001) 3151–3154.

[19] E.J. Maginn, A.T. Bell, D.N. Theodorou, Transport diffusivity of methane in silicalite from equilibrium and nonequilibrium simulations, J. Phys. Chem. 97 (1993) 4173–4181.

[20] A. Heyden, T. Duren, F.J. Keil, Study of molecular shape and non-ideality effects on mixture adsorption isotherms of small molecules in carbon nanotubes: a grand canonical Monte Carlo simulation study, Chem. Eng. Sci. 57 (2002) 2439–2448.

[21] A.I. Skoulidas, D.S. Sholl, Transport diffusivities of CH_4, CF_4, He, Ne, Ar, Xe, and SF_6 in silicalite from atomistic simulations, J. Phys. Chem. B 106 (2002) 5058–5067.

[22] D.A. Reed, G. Ehrlich, Surface diffusion, atomic jump rates and thermodynamics, Surf. Sci. 102 (1981) 588–609.

[23] D.A. Reed, G. Ehrlich, Surface diffusivity and the time correlation of concentration fluctuations, Surf. Sci. 105 (1981) 603–628.

[24] J. Kärger, Random-walk through 2-channel networks-a simple means to correlate the coefficients of anisotropic diffusion in ZSM-5 type zeolites, J. Phys. Chem. 95 (1991) 5558–5560.

[25] R.L. June, A.T. Bell, D.N. Theodorou, Transition-state studies of xenon and SF_6 diffusion in silicalite, J. Phys. Chem. 95 (1991) 8866–8878.

[26] S. Pal, K.A. Fichthorn, Accelerated molecular dynamics of infrequent events, Chem. Eng. J. 74 (1999) 77–83.

[27] C. Tunca, D.M. Ford, A transition-state theory approach to adsorbate dynamics at arbitrary loadings, J. Chem. Phys. 111 (1999) 2751–2760.

[28] B. Smit, L. Loyens, G. Verbist, Simulation of adsorption and diffusion of hydrocarbons in zeolites, Faraday Discuss. (1997) 93–104.

[29] T.J.H. Vlugt, C. Dellago, B. Smit, Diffusion of isobutane in silicalite studied by transition path sampling, J. Chem. Phys. 113 (2000) 8791–8799.

[30] D. Paschek, R. Krishna, Monte Carlo simulations of self- and transport-diffusivities of 2-methylhexane in silicalite, Phys. Chem. Chem. Phys. 2 (2000) 2389–2394.

[31] D. Paschek, R. Krishna, Diffusion of binary mixtures in zeolites: kinetic Monte Carlo versus molecular dynamics simulations, Langmuir 17 (2001) 247–254.

[32] D.R. Garg, D.M. Ruthven, Effect of the concentration dependence of diffusivity on zeolitic sorption curves, Chem. Eng. Sci. 27 (1972) 417–423.

[33] W.E. Schiesser, The Numerical Method of Lines: Integration of Partial Differential Equations, Academic Press, San Diego, 1991.

[34] R. Clift, J.R. Grace, M.E. Weber, Bubbles, Drops and Particles, Academic Press, San Diego, 1978.

[35] S. Sircar, J.R. Hufton, Why does the linear driving force model for adsorption kinetics work?, Adsorption—J. Int. Adsorpt. Soc. 6 (2000) 137–147.

[36] T.J.H. Vlugt, M.G. Martin, B. Smit, J.I. Siepmann, R. Krishna, Improving the efficiency of the configurational-bias Monte Carlo algorithm, Mol. Phys. 94 (1998) 727–733.

[37] Z.M. Du, G. Manos, T.J.H. Vlugt, B. Smit, Molecular simulation of adsorption of short linear alkanes and their mixtures in silicalite, AIChE J. 44 (1998) 1756–1764.

[38] T.J.H. Vlugt, W. Zhu, F. Kapteijn, J.A. Moulijn, B. Smit, R. Krishna, Adsorption of linear and branched alkanes in the silicalite-1, J. Am. Chem. Soc. 120 (1998) 5599–5600.

[39] R. Krishna, B. Smit, T.J.H. Vlugt, Sorption-induced diffusion-selective separation of hydrocarbon isomers using silicalite, J. Phys. Chem. A 102 (1998) 7727–7730.

[40] T.J.H. Vlugt, R. Krishna, B. Smit, Molecular simulations of adsorption isotherms for linear and branched alkanes and their mixtures in silicalite, J. Phys. Chem. B 103 (1999) 1102–1118.

[41] R. Krishna, Exploiting configurational entropy effects for separation of hexane isomers using silicalite-1, Chem. Eng. Res. Des. 79 (2001) 182–194.

[42] S. Calero, B. Smit, R. Krishna, Separation of linear, mono-methyl and di-methyl alkanes in the 5–7 carbon atom range by exploiting configurational entropy effects during sorption on silicalite-1, Phys. Chem. Chem. Phys. 3 (2001) 4390–4398.

[43] S. Calero, B. Smit, R. Krishna, Configurational entropy effects during sorption of hexane isomers in silicalite, J. Catal. 202 (2001) 395–401.

[44] R. Krishna, D. Paschek, Molecular simulations of adsorption and siting of light alkanes in silicalite-1, Phys. Chem. Chem. Phys. 3 (2001) 453–462.

[45] M. Schenk, S.L. Vidal, T.J.H. Vlugt, B. Smit, R. Krishna, Separation of alkane isomers by exploiting entropy effects during adsorption on silicalite-1: a configurational-bias Monte Carlo simulation study, Langmuir 17 (2001) 1558–1570.

[46] B. Smit, R. Krishna, Monte Carlo simulations in zeolites, Curr. Opin. Solid State Mat. Sci. 5 (2001) 455–461.

[47] R. Krishna, B. Smit, Exploiting entropy to separate alkane isomers, Chem. Innov. 31 (2001) 27–33.

[48] R. Krishna, S. Calero, B. Smit, Investigation of entropy effects during sorption of mixtures of alkanes in MFI zeolite, Chem. Eng. J. 88 (2002) 81–94.

[49] R. Krishna, B. Smit, S. Calero, Entropy effects during sorption of alkanes in zeolites, Chem. Soc. Rev. 31 (2002) 185–194.

[50] B. Smit, T.L.M. Maesen, Commensurate freezing of alkanes in the channels of a zeolite, Nature 374 (1995) 42–44.

[51] C.J. Guo, O. Talu, D.T. Hayhurst, Phase-transition and structural heterogeneity—benzene adsorption on silicalite, AIChE J. 35 (1989) 573–578.

[52] D.B. Shah, C.J. Guo, D.T. Hayhurst, Intracrystalline diffusion of benzene in silicalite—effect of structural heterogeneity, J. Chem. Soc. Faraday Trans. 91 (1995) 1143–1146.

[53] P. Szabelski, J. Narkiewicz-Michalek, W. Rudzinski, Coverage dependence of aromatic hydrocarbon diffusion in silicalite: predictions of the three-site lattice model, Appl. Surf. Sci. 196 (2002) 191–201.

[54] B. Millot, A. Methivier, H. Jobic, H. Moueddeb, M. Bee, Diffusion of isobutane in ZSM-5 zeolite: a comparison of quasi-elastic neutron scattering and supported membrane results, J. Phys. Chem. B 103 (1999) 1096–1101.

[55] B. Millot, A. Methivier, H. Jobic, H. Moueddeb, J.A. Dalmon, Permeation of linear and branched alkanes in ZSM-5 supported membranes, Micropor. Mesopor. Mat. 38 (2000) 85–95.

[56] D. Paschek, R. Krishna, Monte Carlo simulations of sorption and diffusion of isobutane in silicalite, Chem. Phys. Lett. 342 (2001) 148–154.

[57] N. Benes, H. Verweij, Comparison of macro- and microscopic theories describing multicomponent mass transport in microporous media, Langmuir 15 (1999) 8292–9299.

[58] J. Kärger, M. Bülow, Theoretical prediction of uptake behaviour in adsorption kinetics of binary gas mixtures using irreversible thermodynamics, Chem. Eng. Sci. 30 (1975) 193–196.

[59] M.J. Sanborn, R.Q. Snurr, Diffusion of binary mixtures of CF_4 and *n*-alkanes in faujasite, Sep. Purif. Technol. 20 (2000) 1–13.

[60] M.J. Sanborn, R.Q. Snurr, Predicting membrane flux of CH_4 and CF_4 mixtures in faujasite from molecular simulations, AIChE J. 47 (2001) 2032–2041.

[61] N. Sundaram, R.T. Yang, Binary diffusion of unequal sized molecules in zeolites, Chem. Eng. Sci. 55 (2000) 1747–1754.

[62] R.T. Yang, Y.D. Chen, Y.T. Yeh, Prediction of cross-term coefficients in binary diffusion: diffusion in zeolite, Chem. Eng. Sci. 46 (1991) 3089–3099.

[63] D. Paschek, R. Krishna, Kinetic Monte Carlo simulations of transport diffusivities of binary mixtures in zeolites, Phys. Chem. Chem. Phys. 3 (2001) 3185–3191.

[64] R. Krishna, Predicting transport diffusivities of binary mixtures in zeolites, Chem. Phys. Lett. 355 (2002) 483–489.

[65] R. Krishna, D. Paschek, Self-diffusivities in multicomponent mixtures in zeolites, Phys. Chem. Chem. Phys. 4 (2002) 1891–1898.

[66] J. Kärger, S. Vasenkov, S.M. Auerbach, Diffusion in zeolites, in: S.M. Auerbach, K.A. Carrado, P.K. Dutta (Eds.), Handbook of Zeolite Science and Technology

(Chapter 10), 19912213–2224.

[67] A. Vignes, Diffusion in binary solutions, Ind. Eng. Chem. Fund. 5 (1966) 189–199.

[68] H.T. Cullinan, Jr., Concentration dependence of the binary diffusion coefficient, Ind. Eng. Chem. Fund. 5 (1966) 281–283.

[69] H.W. Habgood, The kinetics of molecular sieve action. Sorption of nitrogen–methane mixtures by Linde molecular sieve 4A, Can. J. Chem. 36 (1958) 1384–1397.

[70] G.F. Round, H.W. Habgood, R. Newton, A numerical analysis of surface diffusion in a binary adsorbed film, Sep. Sci. 1 (1966) 219–244.

[71] R. Krishna, D. Paschek, Verification of the Maxwell–Stefan theory for tracer diffusion in zeolites, Chem. Eng. J. 85 (2002) 7–15.

[72] R.Q. Snurr, J. Kärger, Molecular simulations and NMR measurements of binary diffusion in zeolites, J. Phys. Chem. B 101 (1997) 6469–6473.

[73] S. Jost, N.K. Bar, S. Fritzsche, R. Haberlandt, J. Kärger, Diffusion of a mixture of methane and xenon in silicalite: a molecular dynamics study and pulsed field gradient nuclear magnetic resonance experiments, J. Phys. Chem. B 102 (1998) 6375–6381.

[74] L.N. Gergidis, D.N. Theodorou, Molecular dynamics simulation of *n*-butane–methane mixtures in silicalite, J. Phys. Chem. B 103 (1999) 3380–3390.

[75] L.N. Gergidis, D.N. Theodorou, H. Jobic, Dynamics of *n*-butane–methane mixtures in silicalite, using quasielastic neutron scattering and molecular dynamics simulations, J. Phys. Chem. B 104 (2000) 5541–5552.

[76] D. Paschek, R. Krishna, Inter-relation between self- and jump-diffusivities in zeolites, Chem. Phys. Lett. 333 (2001) 278–284.

[77] D. Schuring, A.O. Koriabkina, A.M. de Jong, B. Smit, R.A. van Santen, Adsorption and diffusion of *n*-hexane/2-methylpentane mixtures in zeolite silicalite: experiments and modeling, J. Phys. Chem. B 105 (2001) 7690–7698.

[78] M. Heuchel, R.Q. Snurr, E. Buss, Adsorption of CH_4–CF_4 mixtures in silicalite: simulation, experiment, and theory, Langmuir 13 (1997) 6795–6804.

[79] W.J.W. Bakker, Structured systems in gas separation, Ph.D. Thesis, Delft University of Technology, Delft, 1999.

[80] J.M. van de Graaf, Permeation and separation properties of supported silicalite-1 membranes—a modeling approach, Ph.D. Thesis, Delft University of Technology, Delft, 1999.

[81] J.M. van de Graaf, F. Kapteijn, J.A. Moulijn, Modeling permeation of binary mixtures through zeolite membranes, AIChE J. 45 (1999) 497–511.

[82] P.H. Nelson, M. Tsapatsis, S.M. Auerbach, Modeling of permeation through anisotropic zeolite membranes with nanoscopic defects, J. Membr. Sci. 184 (2001) 245–255.

[83] A.L. Myers, J.M. Prausnitz, Thermodynamics of mixed gas adsorption, AIChE J. 11 (1965) 121–130.

[84] S. Sircar, Influence of adsorbate size and adsorbent heterogeneity on IAST, AIChE J. 41 (1995) 1135–1145.

[85] H.W. Dandekar, G.A. Funk, H.A. Zinnen, Process for separating and recovering multimethyl-branched alkanes, US 6069289, Assigned to UOP, 2000.

[86] C.L. Cavalcante, D.M. Ruthven, Adsorption of branched and cyclic paraffins in silicalite. 2. Kinetics, Ind. Eng. Chem. Res. 34 (1995) 185–191.

[87] H.H. Funke, A.M. Argo, J.L. Falconer, R.D. Noble, Separations of cyclic, branched, and linear hydrocarbon mixtures through silicalite membranes, Ind. Eng. Chem. Res. 36 (1997) 137–143.

[88] C.J. Gump, R.D. Noble, J.L. Falconer, Separation of hexane isomers through nonzeolite pores in ZSM-5 zeolite membranes, Ind. Eng. Chem. Res. 38 (1999) 2775–2781.

[89] R. Krishna, D. Paschek, Permeation of hexane isomers across ZSM-5 zeolite membranes, Ind. Eng. Chem. Res. 39 (2000) 2618–2622.

[90] S. Brandani, M. Jama, D.M. Ruthven, Counterdiffusion of *p*-xylene/benzene and *p*-xylene/*o*-xylene in silicalite studied by the zero-length column technique, Ind. Eng. Chem. Res. 39 (2000) 821–828.

[91] O.W. Haas, A. Kapoor, R.T. Yang, Confirmation of heavy-component rollup in diffusion-limited fixed-bed adsorption, AIChE J. 34 (1988) 1913–1915.

[92] L.J.P. van den Broeke, R. Krishna, Experimental verification of the Maxwell–Stefan theory for micropore diffusion, Chem. Eng. Sci. 50 (1995) 2507–2522.

[93] S. Farooq, D.M. Ruthven, Dynamics of kinetically controlled binary adsorption in a fixed-bed, AIChE J. 37 (1991) 299–301.

[94] S. Farooq, D.M. Ruthven, Numerical-simulation of a kinetically controlled pressure swing adsorption bulk separation process based on a diffusion-model, Chem. Eng. Sci. 46 (1991) 2213–2224.

[95] E. Jolimaitre, K. Ragil, M. Tayakout-Fayolle, C. Jallut, Separation of mono- and dibranched hydrocarbons on silicalite, AIChE J. 48 (2002) 1927–1937.